

# The cosmic web connection to the dark matter halo distribution through gravity

F.-S. Kitaura<sup>1,2\*</sup>, A. Balaguera-Antolínez<sup>1,2</sup>, F. Sinigaglia<sup>1,2,3</sup> & M. Pellejero-Ibáñez<sup>4</sup>

<sup>1</sup>*Instituto de Astrofísica de Canarias (IAC), Calle Vía Lactea s/n, 38200, La Laguna, Tenerife, Spain*

<sup>2</sup>*Departamento de Astrofísica, Universidad de La Laguna (ULL), E-38206, La Laguna, Tenerife, Spain*

<sup>3</sup>*Department of Physics and Astronomy, Università degli Studi di Padova, Vicolo dell'Osservatorio 3, I-35122, Padova, Italy*

<sup>4</sup>*Donostia International Physics Centre, Paseo Manuel de Lardizabal 4, 20018 Donostia-San Sebastian, Spain*

Accepted XXX. Received YYY; in original form ZZZ

## ABSTRACT

This work investigates the connection between the cosmic web and the halo distribution through the gravitational potential at the field level. We combine three fields of research, cosmic web classification, perturbation theory expansions of the halo bias, and halo (galaxy) mock catalogue making methods. In particular, we use the invariants of the tidal field and the velocity shear tensor as generating functions to reproduce the halo number counts of a reference catalogue from full gravity calculations, populating the dark matter field on a mesh well into the non-linear regime ( $3 h^{-1} \text{ Mpc}$  scales). Our results show an unprecedented agreement with the reference power spectrum within 1% up to  $k = 0.72 h \text{ Mpc}^{-1}$ . By analysing the three-point statistics on large scales (configurations of up to  $k = 0.2 h \text{ Mpc}^{-1}$ ), we find evidence for non-local bias at the  $4.8 \sigma$  confidence level, being compatible with the reference catalogue. In particular, we find that a detailed description of tidal anisotropic clustering on large scales is crucial to achieve this accuracy at the field level. These findings can be particularly important for the analysis of the next generation of galaxy surveys in mock galaxy production.

**Key words:** large-scale structure of Universe – galaxies: haloes – methods: statistical – methods: analytical

## 1 INTRODUCTION

The cosmic web represents the complex large scale patterns observed in the late time Universe (e.g. Van de Weygaert & Schaap 2009). These are dominated by a filamentary network, connected through knots, which leave large void regions delimited by sheet-like structures. Applications of the cosmic web range from using filaments to study the missing baryons in the inter-galactic medium (Génova-Santos et al. 2015; Eckert et al. 2015; De Graaff et al. 2019), over using voids to study baryon acoustic oscillations (BAOs) (Kitaura et al. 2016a; Liang et al. 2016; Zhao et al. 2020), to study redshift space distortions (RSD) (Chuang et al. 2017; Nadathur et al. 2018), to constrain dark energy (Park & Lee 2007; Lavaux & Wandelt 2010; Bos et al. 2012; Pisani et al. 2015), or to challenge gravity (Kovács et al. 2019). Moreover, the formation of the cosmic web is intricately related to galaxy formation and evolution, which can be studied through the location and orientation of galaxies and their properties in the cosmic web (see e.g. Balogh et al. 2001, 2004; Kauffmann et al. 2004; Blanton et al. 2005; Baldry et al. 2006; Aragón-Calvo et al. 2007b; Lee & Lee 2008; Ball et al. 2008; Libeskind et al. 2012; Beygu et al. 2013; Nuza et al. 2014; Filho et al. 2015; Yang

et al. 2017; Shi & Sheth 2018; Fisher & Faltenbacher 2018; Cui et al. 2019; Alam et al. 2019; Aragon Calvo et al. 2019; Han et al. 2019; Ganeshaiiah Veena et al. 2019). Each cosmic web type has its own theoretical framework and dedicated observing and analysis strategies (Sheth & Van de Weygaert 2004; Van de Weygaert & Bond 2008; Sousbie et al. 2011; Pan et al. 2012; Tempel et al. 2014; Kreckel et al. 2016). Recent studies aim at exploiting the cosmic web to constrain cosmological parameters (Mathuriya et al. 2018; Fang et al. 2019; Naidoo et al. 2019). For all these reasons, understanding and characterising the cosmic web represents one of the major efforts in modern cosmology.

However, the classification of the cosmic web is still arbitrary, and a long standing debate discusses which method is optimal to determine the different types of structures in the matter density field. A comprehensive comparison of the different methods is presented in Libeskind et al. (2018). While there is no doubt about the scientific interest to study the cosmic web, and its usefulness has already been proven, a more quantitative criterion relying on fundamental principles is still missing. The cosmic web is usually directly defined based on the dark matter field. But another approach could consist of defining it based on its tracer, which represents the actual observable. To this end, we focus in this work on the halos hosting the galaxies, which span the cosmic web.

\* E-mail: fkitaura@iac.es

In fact, the theoretical pillars for the current understanding of the formation of halos have been laid long ago, and spectacular progress has been made in the past decades (see [Desjacques et al. 2018](#), and references therein). Their connection to the density field has been thoroughly modelled, and general functional non-linear and non-local dependencies have been studied (see Sec. 2). We suggest therefore to take the perspective of dark matter halos, to revisit the definition of the cosmic web. The accuracy at which we are able to reproduce the summary statistics of the distribution of halos, depending on the specification of the elements, which presumably determine the cosmic web, provides us a measure of the quality of the cosmic web definition itself. This procedure permits us to reduce the number of relevant quantities derived from the gravitational potential to only a few.

A series of papers inspire this work, ranging from the cosmic web definition ([Zeldovich 1970](#); [Bond et al. 1996](#); [Hahn et al. 2007](#)), over the study of halo bias ([Bardeen et al. 1986](#); [Sheth & Tormen 2002](#); [McDonald & Roy 2009](#); [Chan et al. 2012](#)), to the generation of halo catalogues. A precise understanding of halo bias can be key to produce fast and accurate mocks, which then can be used to study systematics in galaxy catalogues, and to put errors bars on the cosmological information (for a variety of mock making methods see ([Bond & Myers 1996](#); [Scoccimarro & Sheth 2002](#); [Monaco et al. 2002a](#); [Kitaura et al. 2014](#); [White et al. 2014](#); [Chuang et al. 2015](#); [Avila et al. 2015](#); [Koda et al. 2016](#); [Izard et al. 2016](#); [Vakili et al. 2017](#); [Stein et al. 2019](#)), and for a comparison between them see ([Chuang et al. 2015](#); [Blot et al. 2019](#); [Lippich et al. 2019](#); [Colavincenzo et al. 2019](#); [Pellejero-Ibañez et al. 2020](#))). In the present work we combine the different fields of research to test in detail, how the cosmic web information can be used within the framework of perturbation theory (PT) halo bias to reproduce the clustering statistics of full gravity calculations.

In the remainder of this paper, we first recap the theoretical background to the classical cosmic web definition, and the general perturbative bias expansion. Subsequently, we present the connection between both, and motivated by that, we propose a new cosmic web classification based on the invariants of the tidal field or velocity shear tensor. Then we briefly describe the reference  $N$ -body simulations and our machine learning approach **BAM**. In the section after, we present numerical studies based on  $N$ -body simulations to quantify the information gain with our proposed cosmic web classification. Finally, we present our conclusions.

## 2 THEORETICAL BACKGROUND

In this section, we revise first the definition of the cosmic web, subsequently the perturbation halo bias, and finally we present a unified picture connecting both.

### 2.1 The cosmic web picture

The cosmic web arises from the growth of structures starting from approximately Gaussian density perturbations (see e.g. [Mo et al. 2010](#)). The connection between the primordial and the final density fluctuations can be described through the mapping between Lagrangian to Eulerian space, which central role is played by the tidal field tensor  $\mathcal{T}_{ij} \equiv \partial_i \partial_j \phi$

constructed from the gravitational potential  $\phi$  with  $i$  and  $j$  standing for different spatial directions (see the pioneering work by [Zeldovich 1970](#)).

Let us start by considering the mapping between the initial (at initial redshift  $z_0$ ) and the final (at final  $z$ ) coordinates of test particles. In Lagrangian perturbation theory this relation is expressed via a displacement field,  $\vec{\psi}(\vec{q})$  (see [Bernardeau et al. 2002](#), for a review):

$$\vec{r} = \vec{q} + \vec{\psi}(\vec{q}), \quad (1)$$

which defines a unique mapping between  $\vec{q}$  and  $\vec{r}$  (usually referred to as Lagrangian and Eulerian coordinates). In addition, one needs to consider the Poisson equation relating the gravitational potential  $\phi$  to the over-density field  $\delta$  through the Laplacian operator:

$$\nabla^2 \phi(\vec{q}) = \delta(\vec{q}), \quad (2)$$

where  $\delta \equiv \rho/\bar{\rho} - 1$ , and  $\rho$  is the (dark) matter density field. If we further assume that the test particles were initially homogeneously distributed, then we can write the following mass conservation relation:

$$\rho(\vec{r}) d\vec{r} = \langle \rho(z_0) \rangle d\vec{q}. \quad (3)$$

The inverse of the Jacobian of the coordinate transformation defines the over-density field:

$$1 + \delta(\vec{r}(\vec{q})) = J(\vec{q})^{-1}, \quad (4)$$

with

$$J(\vec{q}) \equiv \left| \frac{\partial \vec{r}}{\partial \vec{q}} \right|. \quad (5)$$

The displacement field is given by the gradient of a potential (since any initial curl decays with cosmic evolution considering up to second order Lagrangian perturbation theory)  $\vec{\psi}(\vec{q}) = -\nabla \phi(\vec{q})$ , and hence Eq. (4) can be rewritten as:

$$1 + \delta(\vec{q}) = \left| \delta_{ij}^K + \partial_i \partial_j \phi(\vec{q}) \right|^{-1}. \quad (6)$$

We can define the tidal field, strain, or deformation tensor

$$\mathcal{T}_{ij}(\vec{q}) \equiv \partial_i \partial_j \phi(\vec{q}), \quad (7)$$

which is symmetric, allowing us to diagonalize it with eigenvalues  $\lambda_1 \geq \lambda_2 \geq \lambda_3$ . This permits us to rewrite Eq. (6) as:

$$1 + \delta(\vec{q}) = [(1 - \lambda_1(\vec{q}))(1 - \lambda_2(\vec{q}))(1 - \lambda_3(\vec{q}))]^{-1}, \quad (8)$$

Linearly expanding Eq. (8) we obtain the linear density field in Lagrangian coordinates:  $\delta(\vec{q}) \equiv \lambda_1(\vec{q}) + \lambda_2(\vec{q}) + \lambda_3(\vec{q})$ . By linearising Eq. (6) we obtain the Zel'dovich approximation:

$$\delta(\vec{q}) \simeq -\nabla \cdot \vec{\psi}(\vec{q}). \quad (9)$$

The Zel'dovich approximation is often identified with Eq. (8), instead of linear Lagrangian perturbation theory, as we do here with Eq. (9). However, Eq. (8) is more general and led to a structure formation model (which we discuss below) and admits higher order Lagrangian perturbation theory expressions ([Bouchet et al. 1992](#); [Buchert & Ehlers 1993](#); [Buchert 1994](#); [Bouchet et al. 1995](#); [Catelan 1995](#); [Betancort-Rijo & López-Corredoira 2000](#)). In the approximation of curl-free velocity fields, they can be directly inferred from the normalised divergence of the density field

$$\theta(\vec{r}) \equiv -(a H(a) d \ln D(a) / d \ln a)^{-1} \nabla \cdot \vec{v}(\vec{r}). \quad (10)$$

In the linear velocity approximation  $\theta = \delta$ . From an Eulerian perspective, one needs to consider the inverse mapping  $\vec{q} = \vec{r} - \vec{\psi}(\vec{q}(\vec{r}))$  (Kitaura & Angulo 2012), which under mass conservation yields the inverse Jacobian:  $J'(\vec{r}) \equiv \left| \frac{\partial \vec{q}}{\partial \vec{r}} \right|$ , and hence to  $1 + \delta(\vec{r}) = |\delta_{ij}^K - \partial_i \partial_j \phi(\vec{r})|$ . Once shell crossing allows for multi-streaming (e.g. Hahn et al. 2015), there is no unique solution without the peculiar velocity information, unless some approximation is done to ensure reversibility (e.g. Nusser & Dekel 1992; Gramann 1993; Kitaura & Angulo 2012; Shi et al. 2018), some optimisation is applied (e.g. Peebles 1989; Nusser & Branchini 2000; Frisch et al. 2002), or an ensemble of solutions in a statistical sense is sought (e.g. Kitaura 2013; Jasche & Wandelt 2013; Wang et al. 2013).

In the linear regime one obtains the same approximations, as given by Eqs. (8) and (9), substituting the  $\vec{q}$ -coordinates with the  $\vec{r}$ -coordinates dependence. For what matters, the same theoretical grounds are valid, and from now on, we consider the tidal field tensor expressed in Eulerian coordinates.

In particular, the density field in Eulerian coordinates (computed from the non-linear gravitational potential) reads:

$$\delta(\vec{r}) \equiv \lambda_1(\vec{r}) + \lambda_2(\vec{r}) + \lambda_3(\vec{r}). \quad (11)$$

The result shown in Eq. (8) led to the top-down scenario of structure formation, in which the catastrophies of infinite density occurred first along the largest eigenvalue to first form sheets also known as Zel'dovich "pancakes", then along the second largest to form filaments, and finally along the smallest eigenvalue to form knots (Hidding et al. 2014; Feldbrugge et al. 2018).

This is in contrast with the well established hierarchical model scenario, in which smaller objects form first and by merging processes grow to larger ones (Press & Schechter 1974; Fry & Peebles 1978; White & Rees 1978; Bardeen et al. 1986). In fact, Eq. (8) can be used to compute gravitational collapse with LPT and combined with the hierarchical model to generate halo distributions including accurate merger histories (Bond & Myers 1996; Monaco et al. 2002b). Bond et al. (1996) investigated both scenarios studying the appearance of sheets ("pancakes") as compared to filaments in both  $N$ -body and Zel'dovich calculations, finding a preference for the latter. That paper coined the term cosmic-web, and used arguments based on eigenvalues of the shear of the velocity field

$$\Sigma_{ij} \equiv \frac{1}{2} (\partial_i v_j + \partial_j v_i) \quad (12)$$

(which is equivalent to the tidal field in linear theory) to make a cosmic web classification. They considered the ellipticity  $e \propto (\lambda_1 - \lambda_3)$  and the prolateness  $p \propto (\lambda_1 + \lambda_3 - 2\lambda_2)$  (both up to a consistent normalisation of typically  $2\delta$ ) to define filaments:  $p \sim -e$  and sheets:  $p \sim e$ , which imply  $\lambda_1 \sim \lambda_2$  and  $\lambda_2 \sim \lambda_3$ , respectively. A more systematic cosmic web classification, also inspired by the Zeldovich "pancakes" formation, was introduced by Hahn et al. (2007), commonly known as the T-web. In this classification, they considered knots, as the regions in which gravitational collapse causes matter inflow expressed through positive eigenvalues (knots:  $\lambda_1, \lambda_2, \lambda_3 > 0$ ); voids as opposed to knots are described as expanding regions with negative eigenvalues (voids:  $\lambda_1, \lambda_2, \lambda_3 < 0$ ); filaments being closer to knots are defined as regions with two positive eigenvalues, and a

negative one (filaments:  $\lambda_1, \lambda_2 > 0; \lambda_3 < 0$ ); while sheets are defined by one positive, and two negative eigenvalues (sheets:  $\lambda_1 > 0; \lambda_2, \lambda_3 < 0$ ). The cases in which any eigenvalue coincides with zero has been neglected, as it can be arbitrarily assigned to any limiting case. We note, that this picture coincides with the one provided by (Bond et al. 1996), since also in the T-web definition filaments have the largest eigenvalues closer to each other, while for sheets this happens for the lowest ones.

These definitions, however are more qualitative than quantitative, since there is not a first principle guaranteeing that a filament is really such a cosmic web type. In fact, this cosmic web classification depends on the smoothing scale, mesh resolution, and mass assignment scheme. To alleviate this, an eigenvalue threshold (instead of zero) was introduced (Forero-Romero et al. 2009), and a multi-scale classification was developed (Aragón-Calvo et al. 2007a; Cautun et al. 2013). Alternatively, the velocity shear tensor has been revived to classify the cosmic web (V-web: Hoffman et al. 2012), applying the same classification, as in (Hahn et al. 2007) with comparable results (Nuza et al. 2014). Certainly, beyond the linear velocity-density relation, the velocity shear carries complementary information to the tidal field tensor (see Sec. 2.2). The tidal field has also been used to compute the spine of the cosmic web (Sousbie et al. 2008; Aragón-Calvo et al. 2010; Feldbrugge et al. 2018). Another perspective to the cosmic web is based on folding of phase-space (Vogelsberger et al. 2008; White & Vogelsberger 2009; Vogelsberger & White 2011; Shandarin et al. 2012; Abel et al. 2012; Falck et al. 2012). The dark matter distribution can be regarded as a continuous field, and gravitational collapse as foldings of phase-space, every time shell crossing occurs. In this framework, voids are regions in which shell crossing has not happened yet, and according to the number of shell-crossings, or the number of axis across which shell-crossing happens, the different cosmic web structures can be identified. As shown in a series of recent works, the regions of shell-crossing, i.e., the caustics or catastrophies, can be computed from the eigenvalues and eigenvectors of the tidal field tensor (Arnold et al. 1982; Hidding et al. 2014; Feldbrugge et al. 2018).

## 2.2 The halo bias picture

On the other hand, the bias of galaxies, galaxy clusters, and halos with respect to (w.r.t.) the underlying dark matter field has been studied since long in galaxy surveys and numerical simulations (e.g. Press & Schechter 1974; White & Rees 1978; Kaiser 1984; Peacock & Heavens 1985; Bardeen et al. 1986; Szalay 1988; Feldman et al. 1994; Mo & White 1996; Sheth & Tormen 1999; Kravtsov & Klypin 1999; Seljak 2000; Cooray & Sheth 2002; Tinker et al. 2010; Valageas 2011). It has been established that the bias relation is non-linear, stochastic, and scale-dependent (e.g. Peebles 1980; Saslaw & Hamilton 1984; Fry & Gaztanaga 1993; Cen & Ostriker 1993; Bernardeau 1994; Sheth 1995; Dekel & Lahav 1999; Sheth & Lemson 1999; Somerville et al. 2001; Casas-Miranda et al. 2002; Smith et al. 2007; Desjacques et al. 2010; Scoccimarro et al. 2012; Baldauf et al. 2013; Schmidt et al. 2013; Kitaura et al. 2014; Neyrinck et al. 2014; Ahn et al. 2015). Furthermore, it also depends on the history each volume element of the Universe has experienced (e.g. Gao & White 2007; Angulo et al. 2008; Lazeyras et al. 2017; Chue et al. 2018;

(Contreras et al. 2019). This so-called assembly bias can be expressed in terms of the tidal field tensor, of the velocity field, and of some sort of short-range density dependence, which altogether also account for non-local bias (Matsubara 1999; McDonald 2006; Matsubara 2008; Scoccimarro et al. 2012; Chan et al. 2012; Baldauf et al. 2012, 2013; Sheth et al. 2013; Pajer & Zaldarriaga 2013; Schmidt et al. 2013; Porto et al. 2014; Saito et al. 2014; Assassi et al. 2014; Senatore & Zaldarriaga 2015; Angulo et al. 2015a; Mirbabayi et al. 2015; Senatore 2015; Modi et al. 2017; Lazeyras & Schmidt 2018; Abidi & Baldauf 2018; Munshi 2018).

We investigate an effective bias model at the Eulerian field level (Schmittfull et al. 2019) restricted to the following dependencies between the halo field  $\delta_h$  and the dark matter (DM) gravitational potential:

$$\delta_h(\vec{r}) \propto P(\delta_h(\vec{r})|\nabla^2\phi(\vec{r}), \partial_i\partial_j\phi(\vec{r})) = P(\delta_h|\delta, \mathcal{T}). \quad (13)$$

This relation is not truncated to any order, but effectively corresponds to resummed perturbation theories (see e.g. Elia et al. 2011), including the infinite non-linear expansion of  $\delta$  and the tidal anisotropies to higher orders, as we show in this work (see also §2.2 and Pellejero-Ibañez et al. (2020)).

This work is especially inspired by McDonald & Roy (2009) and Chan et al. (2012). In these works, the halo-bias terms are constructed from the tidal field tensor  $\mathcal{T}$  and the velocity shear  $\Sigma_{ij}$ . For a modern and accurate description of both the two and three-point statistics of biased tracers of the large-scale structure based on perturbation theory see Eggemeier et al. (2021) and other recent works such as Lazeyras & Schmidt (2018). As mentioned before, in the linear regime, and in the absence of vorticity of the velocity field (washed away due to the cosmological expansion, see e.g. Bernardeau et al. 2002) the velocity shear and the tidal field tensor coincide.

The tidal field can be identified among the precursors of the so-called assembly bias (e.g. Gao & White 2007; Angulo et al. 2008; Lazeyras et al. 2017; Chue et al. 2018). Indeed, tidal torque theory (Doroshkevich 1970; Binney & Silk 1979; White 1984; Barnes & Efstathiou 1987; Hoffman 1988; Heavens & Peacock 1988; Catelan & Theuns 1996a,b; Porciani et al. 2002a,b; Lu et al. 2009; Cusin et al. 2017) predicts an angular momentum of proto-halos of the form (White 1984)  $L_i \propto \epsilon_{ijk}^{\text{LC}} \mathcal{T}_{j\ell} \mathcal{I}_{\ell k}$ , where  $\mathcal{I}_{ij} \propto \int_V d^3q q_i q_j$  denotes the inertia tensor of the mass contained in the volume  $V$  (with  $\epsilon_{kij}^{\text{LC}}$  being the Levi-Civita tensor). This represents the seeds of the spin of dark matter halos, as well as anisotropies in the environment (Ramakrishnan et al. 2019) inducing to different clustering signals of present-day haloes. Furthermore, the late cosmological times, this can induce curl in the velocity field  $\omega_i \propto \epsilon_{ijk}^{\text{LC}} \partial_j v_k$ , with non negligible impact in the formation of dark matter halos (Pichon & Bernardeau 1999; Hahn et al. 2015).

As pointed out by (McDonald & Roy 2009), short-range non-local bias at a given scale  $R$  can be modelled by a series

of higher order derivative terms like  $R^n \nabla^n \delta$  (such as  $n = 2$ ) (see also Werner & Porciani 2020). Cosmic voids can be described, as such a case of short range non-local bias, where the density field curvature changes on relatively small scales (Chuang et al. 2017). Also, the local tidal environment has been studied with a tensor of the form:  $\partial_i \partial_j \delta$  (Heavens & Peacock 1988). Let us summarise all these short range non-local bias terms by  $\Gamma_{ij}^l = \partial_i^l \partial_j^l \delta$  for  $i = j$ ,  $i \neq j$ , and  $l \in \mathbb{N}$ . The mixed terms with  $i \neq j$  have been considered in many other works. They enter at higher orders than the  $\nabla^2 \delta$  term, but are relevant for the bi-spectrum (see for example, Desjacques et al. 2018; Nadler et al. 2018; Eggemeier et al. 2019; Fujita & Vlah 2020; Eggemeier et al. 2021). There are also approaches that measure the various perturbative galaxy bias ingredients from simulations, which means they also contain all non-linearities (Kokron et al. 2021; Zennaro et al. 2021).

In addition, the halo distribution represents a discrete realisation of the expected number counts of objects per volume element. This causes a stochastic uncertainty component, which can be modelled by an additive shot-noise term in the power spectrum measurements (Feldman et al. 1994). In large scale structure analysis this uncertainty can be modelled by a white noise term. We refer to the general stochastic bias component as  $\epsilon$ .

In summary, the halo bias model would have the following dependencies:

$$\delta_h(\vec{r}) = F(\delta, \mathcal{T}, \Gamma, \Sigma, \omega, \epsilon). \quad (14)$$

We consider each dependency grouped in separated dependencies, such as the combined local and non-local density dependence.

Since the halo number density is a scalar quantity any non-local bias term needs to be some kind of contraction of a tensor. In particular, let us consider the series of higher order non-local bias terms constructed based upon  $\mathcal{T}_{ij}$ , and rewrite the convenient trace-less tensor as

$$s_{ij}(\vec{r}) \equiv \mathcal{T}_{ij} - \frac{1}{3} \delta_{ij}^K \delta(\vec{r}). \quad (15)$$

The corresponding second-order and third order bias terms are respectively given by the following contractions:  $s^2 \equiv s_{ij} s_{ji}$ ,  $s^3 \equiv s_{ij} s_{kj} s_{ki}$ . We consider a general local and non-local functional dependence on the density field  $F_{\delta, \mathcal{T}}(\delta) \equiv F_{\delta}(\delta, \mathcal{T}_{ij})$ .

We note that the velocity terms considered in (McDonald & Roy 2009) correspond to  $F_{\text{shear}}(\vec{v}|_{\text{curl-free}})$  for curl-free fields, there is an additional shear field for the divergence-free field  $F_{\text{shear}}(\vec{v}|_{\text{div-free}})$ , according to the Helmholtz decomposition (Bladel 1959). Also, the curl of the divergence free velocity field does not vanish and additional terms can be constructed. Additionally, we group the short-range density terms by  $F_{\delta\text{SR}}(\partial_i^l \partial_j^l \delta(\vec{r}))$ , and all the noise terms in  $F_{\epsilon}(\epsilon(\vec{r}))$ .

The resulting Taylor expanded bias dependence following McDonald & Roy (2009) to model the halo over-density in Eulerian coordinates  $\vec{r}$  is given by:

$$\begin{aligned}
\delta_{\text{h}}(\vec{r}) = & \underbrace{\underbrace{c_{\delta}\delta(\vec{r})}_{\text{local}}}_{\text{first order}} + \underbrace{\underbrace{\frac{1}{2}c_{\delta^2}(\delta^2(\vec{r}) - \langle\delta^2\rangle)}_{\text{local}} + \underbrace{\frac{1}{2}c_{s^2}\left(s^2(\vec{r}) - \frac{2}{3}\langle\delta^2\rangle\right)}_{\text{non-local}}}_{\text{second order}} + \underbrace{\underbrace{\frac{1}{3!}c_{\delta^3}\delta^3(\vec{r})}_{\text{local}} + \underbrace{\frac{1}{2}c_{\delta s^2}\delta(\vec{r})s^2(\vec{r}) + \frac{1}{3!}c_{s^3}s^3(\vec{r})}_{\text{non-local}}}_{\text{third order}} + \underbrace{\mathcal{O}(F_{\delta,\mathcal{T}}(\delta)|^4)}_{\text{local \& non-local}} \\
& \underbrace{\hspace{15em}}_{\text{curl-free \& } \theta=\delta \text{ terms}} \\
& + \underbrace{\underbrace{F_{\delta\text{SR}}(\partial_i^l\partial_j^l\delta(\vec{r}))}_{\text{short range } \theta=\delta \text{ terms } l\in\mathbb{N}}}_{\text{first order+}} + \underbrace{\underbrace{F_{\text{shear}}(\vec{v}(\vec{r})|_{\text{curl-free}})}_{\text{non-local}} + \underbrace{F_{\text{shear}}(\vec{v}(\vec{r})|_{\text{div-free}})}_{\text{non-local}} + \underbrace{F_{\text{curl}}(\vec{v}(\vec{r}))}_{\text{non-local}}}_{\text{third order+}} + \underbrace{\underbrace{F_{\epsilon}(\epsilon(\vec{r}))}_{\text{local \& non-local}}}_{\text{noise terms}}}_{\text{first order+}}, \quad (16)
\end{aligned}$$

where  $\delta$  stands for the dark matter field, the  $c_s$  are some bias factors, the  $s^2$  and  $s^3$  are non-local bias terms derived from the tidal field tensor, and  $\theta$  is the weighted velocity divergence. We neglect in this study the velocity terms and the short range terms, which are typically given for  $l = 1$  and  $i = j$  (Chuang et al. 2017; Werner & Porciani 2020), although also  $i \neq j$  has been considered (Heavens & Peacock 1988). It is important to stress that in contrast to the majority of previous works (see e.g. Bardeen et al. 1986; Sheth & Tormen 2002; McDonald & Roy 2009; Chan et al. 2012), we consider the gravitational potential from the cosmologically evolved non-linear density field defined on a few Mpc scales. At such scales the divergence-free component makes up only a few percent of the curl-free component, and becomes increasingly important towards sub-Mpc scales (Kitaura et al. 2012). Thus, we can assume approximately curl-free local density terms, and the first row can be identified with the tidal shear for curl-free fields with  $\theta = \delta$ :  $F_{\delta,\mathcal{T}}(\delta) \simeq F_{\text{shear}}(\vec{v}(\vec{r})|_{\text{curl-free}}^{\theta=\delta})$ .

We are interested in practical applications to efficiently generate mock galaxy catalogues saving the expensive costs of running  $N$ -body simulations. For this reason, we can, a priori, not assume to have such a precise velocity field to be able to consider the case for which  $\theta \neq \delta$ . However, we can assume that machine learning algorithms can efficiently deliver such precise velocity fields (see e.g. Wu et al. 2021). We will, hence, also consider the velocity shear as in the pioneering work of Bond et al. (1996) to describe the halo distribution. Below, we will start with the tidal field tensor, but the same analysis will be shown for the velocity shear tensor in §5.1.1.

### 2.3 Unified cosmic web and halo bias picture

The gravitational potential is the key ingredient in both the development of the cosmic web and the bias relation between the halo field and the underlying dark matter density field. Therefore, following (Sheth & Tormen 2002; Chan et al. 2012), we analyse the gravitational deformation tensor in terms of its invariants (see also Munshi 2018). The corresponding eigenvalues of the symmetric tidal tensor  $\mathcal{T}$  are computed by solving its cubic characteristic polynomial (see e.g. Schröder et al. 2010):  $\det(\lambda\mathbb{1} - \mathcal{T}) = \lambda^3 - I_1\lambda^2 + I_2\lambda - I_3 =$

0, with invariants:

$$\begin{aligned}
I_1 & \equiv \text{tr}(\mathcal{T}) = \lambda_1 + \lambda_2 + \lambda_3 \equiv \delta \text{ with } \lambda_1 \geq \lambda_2 \geq \lambda_3, \\
I_2 & \equiv \frac{1}{2}(\text{tr}^2(\mathcal{T}) - \text{tr}(\mathcal{T}^2)) = \lambda_1\lambda_2 + \lambda_1\lambda_3 + \lambda_2\lambda_3, \\
I_3 & \equiv \det(\mathcal{T}) = \lambda_1\lambda_2\lambda_3, \\
I_4 & \equiv \text{tr}(\mathcal{T}^t\mathcal{T}) = \lambda_1^2 + \lambda_2^2 + \lambda_3^2 = I_1^2 - 2I_2, \\
I_5 & \equiv \text{tr}(\mathcal{T}^t\mathcal{T}^t\mathcal{T}) = \lambda_1^3 + \lambda_2^3 + \lambda_3^3 \\
& = I_1^3 - 3I_1I_2 + 3I_3 = I_1I_4 - I_1I_2 + 3I_3. \quad (17)
\end{aligned}$$

Defining  $9\alpha \equiv I_1^2 - 3I_2 = I_4 - I_2$ ,  $\beta \equiv (-9I_1I_2 + 27I_3 + 2I_1^3)/54$ , and  $\Theta \equiv \cos^{-1}(\beta/\sqrt{\alpha^3})/3$ , it is possible to formulate the eigenvalues as (Weisstein 2002; Press et al. 2007; Nickalls 1993):  $\lambda_1 = I_1/3 + 2\sqrt{\alpha}\cos(\Theta)$ ,  $\lambda_2 = I_1/3 + 2\sqrt{\alpha}\cos(\Theta - 2\pi/3)$ , and  $\lambda_3 = I_1/3 + 2\sqrt{\alpha}\cos(\Theta + 2\pi/3)$ . From this, the moments can be constructed (Pierpaoli & Basser 1996):  $\mu_1 = \langle\lambda_i\rangle = I_1/3$ ,  $\mu_2 = \langle(\lambda_i - \mu_1)^2\rangle = 2\alpha$ , and  $\mu_3 = \langle(\lambda_i - \mu_1)^3\rangle = 2\beta$ . The second order non-local bias  $s^2$  term (see McDonald & Roy 2009) is also related to  $\alpha$  (Paranjape et al. 2018):  $s^2 = 6\alpha$ . Hence,  $s^2 = 2/3(I_4 - I_2) = I_4 - 1/3I_1^2$ . In the same way  $s^3$  is related to  $\mu_3$ :  $s^3 = 3\mu_3 = 6\beta = -I_1I_2 + 3I_3 + 2/9I_1^3 = 1/3(I_5 - 1/3I_1^3) + 2I_3$ . The difference among the eigenvalues induces a non vanishing  $\alpha$ , eventually also causing an ellipticity  $e \equiv (\lambda_1 - \lambda_3)/(2\delta)$  and a prolateness  $p \equiv (\lambda_1 + \lambda_3 - 2\lambda_2)/(2\delta)$ , which require knowledge on the first three invariants (Chan et al. 2012):  $I_2 = I_1^2/3(1 - (3e^2 + p^2))$  and  $I_3 = I_1^3/27(1 - p)[(1 + p)^2 - 9e^2]$ . Following (Chan et al. 2012) we can find the relation between the halo bias terms from McDonald & Roy (2009) and the invariants, as generating functions), respectively (see §2.2). From Eq. (17) it is clear that each of the eigenvalues can be expressed as a function of the first three invariants. As a consequence, the classical cosmic web classification, dubbed T-web, (based on combinations of conditions on the eigenvalues to obtain four different cosmic web types:  $t_{\text{cw}} = \{\text{knot, filament, sheet, void}\}$ , see (Hahn et al. 2007)) has an equivalent formulation in terms of conditions on the invariants, as we show in the appendix A.

### 3 GRAVITY CALCULATIONS WITH NUMERICAL SIMULATIONS

We rely in this work on the Minerva suite (Grieb et al. 2016), which consist on a set of 300  $N$ -body dark matter only simulations, each embedded in a cubic box of  $L_{\text{box}} = 1.5h^{-1}$  Gpc side using  $1000^3$  particles. Dark matter haloes are identified with a standard Friends-of-Friends (FoF) algorithm at

redshift  $z = 1$ , and subjected to an unbinding procedure (Springel et al. 2001), in which particles with positive total energy are removed and halos artificially linked by FoF are separated. The minimum halo mass is  $\sim 2.7 \times 10^{12} h^{-1} M_{\odot}$ . The advantage of these simulations is that they have been thoroughly studied in the different summary statistics (Blot et al. 2019; Balaguera-Antolínez et al. 2020), and thus constitute an ideal reference set.

This population of halos is particularly sensitive to a well modelling of non-local bias in the three-point statistics. Luminous Red Galaxies, correspond to an effective higher mass cut ( $> 10^{13} h^{-1} M_{\odot}$ ), and thus the corresponding halos better trace the peaks of the density field. These can be described with simpler bias models (Kitaura et al. 2015, 2016b). Although, in these studies the bi-spectra were not reproduced to the accuracy presented in this work. On the other hand considering very low mass halos ( $> 10^8 h^{-1} M_{\odot}$ ) brings the halo field closer to the dark matter field, and no strong evidence for non-local bias terms was found (Pellejero-Ibañez et al. 2020). The rather intermediate halo mass cut considered in this study constitutes the most challenging one, and hitherto no well modelling of the three-point statistics has been found on the scales relevant to baryon acoustic oscillations, or redshift space distortions (see Balaguera-Antolínez et al. 2020). A good handling on halo masses above  $10^{11}$  and below  $10^{13} h^{-1} M_{\odot}$  is critical for the upcoming surveys focusing on emission line galaxies, such as (Levi et al. 2013; Amendola et al. 2016; Benitez et al. 2014; De Jong et al. 2019).

Since, we aim at studying the relation between the formation of compact small scale objects and the large scale structure, we define a regular mesh (with cell center positions at  $\vec{r}$ ) of  $500^3$  cells, which implies a  $3 h^{-1}$  Mpc cell side resolution. We apply nearest-grid-point to the halo catalogue and to the dark matter particles, to produce halo number counts per cell  $N_{\text{h}}(\vec{r})$  and the dark matter field  $\delta(\vec{r})$ , respectively.

The cell size has been chosen to be large enough that there is a considerable computing gain, but small enough that it is still below the scale of typical displacements to avoid an additional smoothing which could have an impact on Baryon Acoustic Oscillations or Redshift Space Distortions. A deeper study in this direction should be performed to investigate whether even smaller resolution meshes can be safely considered at the expense of requiring more computing resources.

#### 4 BAM: A MACHINE LEARNING METHOD TO COMBINE GENERATING FUNCTIONS

The BAM method represents a physically motivated supervised machine learning algorithm in which the cost function based on the power spectrum of the respective targeted variables is minimized with non-linear and non-local isotropic kernels and anisotropic explicit bias dependencies. The kernels preserve dimensionality and are iteratively extracted from the reference simulation.

The bi-spectrum is not explicitly used in the calibration process. Nevertheless, using an accurate dark matter field above a certain scale (a few Mpc) combined with an accurate bias modelling ensures a precise three-point statistics of the tracer distribution (see Kitaura et al. 2015). As in all previous works using the BAM algorithm, we describe the joint proba-

bility distribution of the number of halos and all considered properties (see Balaguera-Antolínez et al. 2020).

In this work, we use in the calibration process a down-sampled version of the initial conditions and the final catalogue from the reference simulation.

Considering the general problem of a quantity  $q$  determined by the functional dependence on a series of variables, which are generating functions  $\{\eta_1, \eta_2, \dots\}$ :  $q = F(\eta_1, \eta_2, \dots)$ , with each variable having a potentially non-linear and non-local relation w.r.t.  $q$ :  $q = F_i(\eta_i) \forall i$ . Let us further assume that we have a method to express the dependence, as combinations of non-linear expansions of each variable:

$$\begin{aligned} q &= c_1 F_1(\eta_1) + c_2 F_2(\eta_2) + c_{12} F_{12}(\eta_1 \eta_2) + \dots \\ &= c_1 (a_1 \eta_1 + a_2 \eta_1^2 + \dots) + c_2 (b_1 \eta_2 + b_2 \eta_2^2 + \dots) + \dots \end{aligned} \quad (18)$$

If there is then a relationship between the different variables:  $v_i = f_i(\{\eta_j : j \neq i\})$ , the question arises of which is the minimum number of variables, which fully constrains  $q$ . In practice, it is difficult to implicitly include cross terms such as  $F_{12}(\eta_1 \eta_2)$ . The reason is that a particular finite binning must be used to describe each quantity  $\eta_i$ . Hence, cross products are usually not well modelled by the original binning of each component. Therefore, a higher accuracy is achieved when those cross terms are explicitly included.

#### 4.1 Technical details of the BAM algorithm

Our particular science case consists of reproducing the halo number counts per cell  $N_{\text{h}}$  on a mesh of an  $N$ -body simulation as a function of variables (see e.g. Kitaura et al. 2014).

It is important to note, that the BAM code used in this work does not truncate the bias relation to any order, but effectively corresponds to resummed perturbation theories (see e.g. Elia et al. 2011), including the infinite non-linear expansion of  $\delta$  and the tidal anisotropies to higher orders, as we show in this work. This has already been studied to some extent (depending on  $\delta$  and  $\delta$ +T-web) in Balaguera-Antolínez et al. (2019); Pellejero-Ibañez et al. (2020).

The BAM algorithm takes a set of binned variables  $\{\eta\}$  and measures from the reference simulation the probability distribution  $P(N_{\text{h}}|\{\eta\})$  for halo number counts per cell  $N_{\text{h}}$  conditional to the set  $\{\eta\}$ . This conditional probability distribution function represents the joint stochastic and deterministic halo bias expressed in terms of the chosen set of variables.

In other words, the noise terms encoded in Eq. (16) through  $F_{\epsilon}(\epsilon(\vec{r}))$  are all effectively included in our study. BAM then goes through each cell  $i$  in the mesh looking up the joint set of (binned) variables  $\{\eta\}_i$  corresponding to that cell, and randomly selects a halo number count  $N_{\text{h}}$  from the available probabilistic relation  $P(N_{\text{h}}|\{\eta\})$ . This relation however, depends on the definition of the dark matter density field  $\delta$  on the mesh, from which all invariants are derived. But the definition of  $\delta$  is arbitrary, and does not coincide with the way in which the dark matter distribution was used to define the halos (Springel et al. 2001). There is an effective kernel relating the mass assignment scheme used to define the density field on the mesh and the halo finder used to define the halos. In addition, all the missing contributions to the bias (for instance short range non-local bias) can potentially have an impact on the power spectrum. For all these reasons, BAM applies a kernel to the dark matter density. This kernel

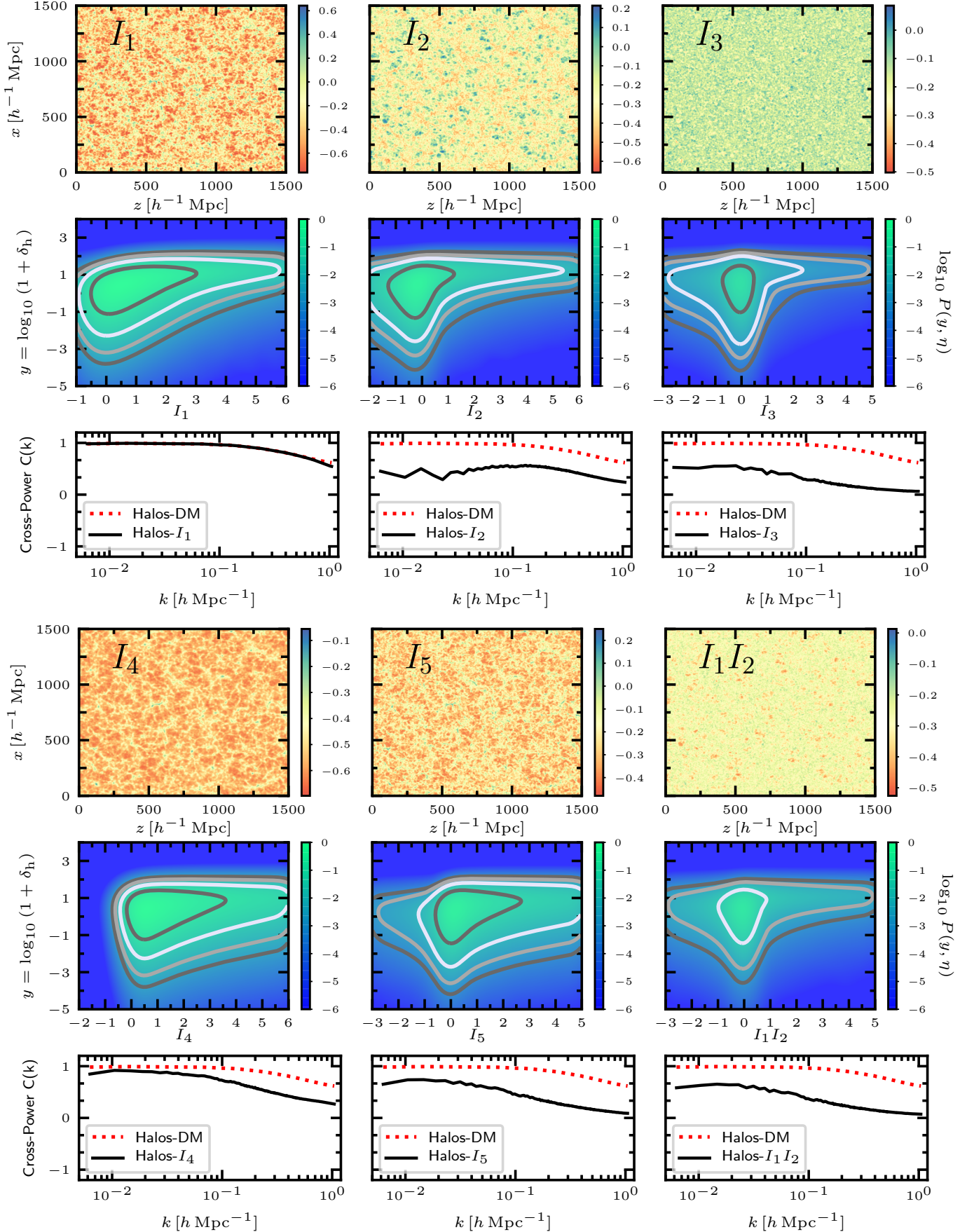


**Figure 1.** Generating functions  $\{I_1, I_2, I_3, I_4, I_5, I_1 I_2\}$  and their relation to the halo field extracted from  $N$ -body simulations. Upper panels show slices through the  $1.5 h^{-1}$  Gpc side volume for each variable. The second row shows the smoothed bias relation with respect to the halo number over-density. The contours in each panel denote the region containing 65, 95 and 99% of the total number of classified cells. The lower panels show the corresponding cross power spectra.

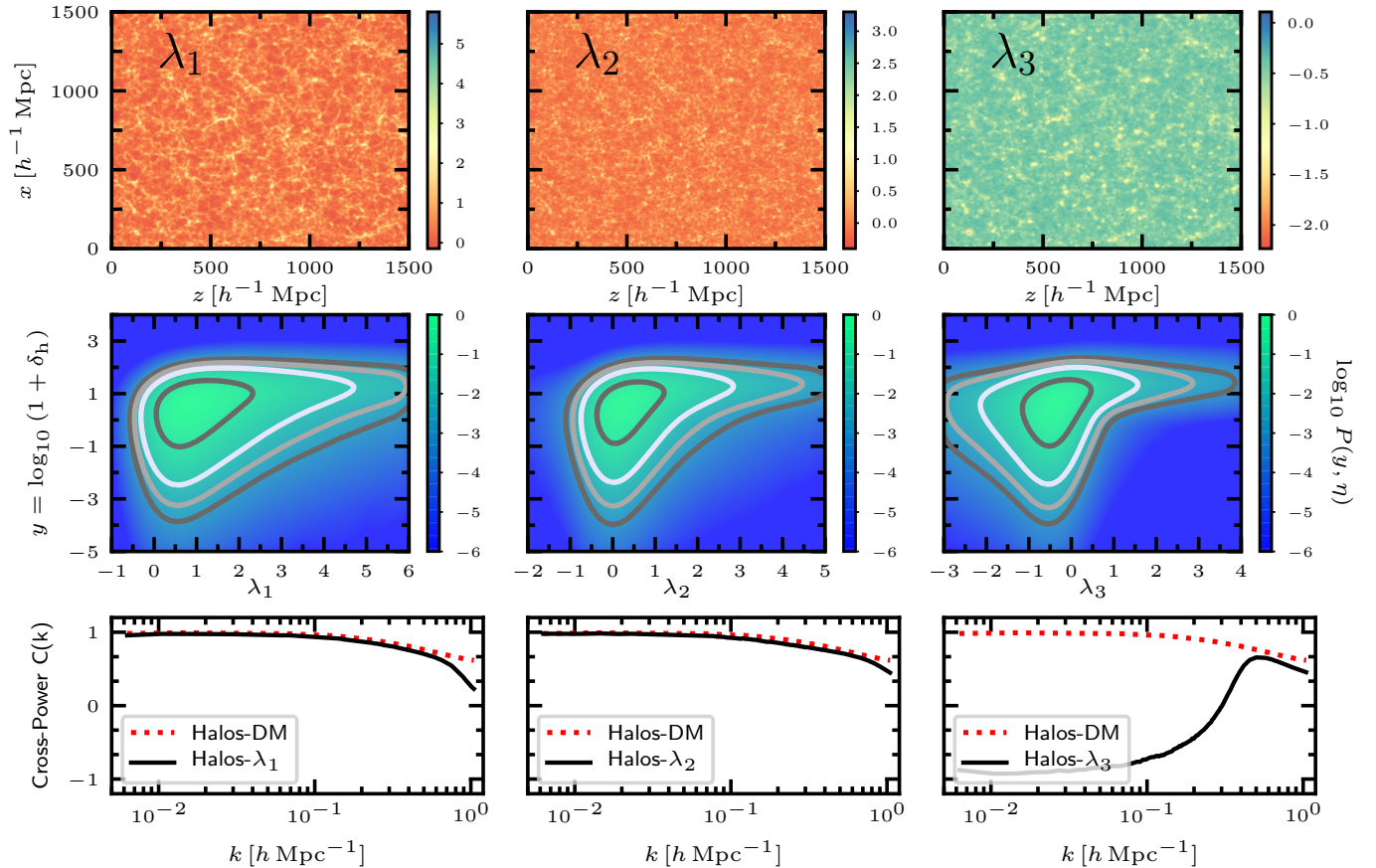


**Figure 2.** Generating functions  $\{\lambda_1, \lambda_2, \lambda_3\}$  and their relation to the halo field extracted from  $N$ -body simulations. Upper panels show slices through the  $1.5 h^{-1}$  Gpc side volume for each variable. The second row shows the smoothed bias relation with respect to the halo number over-density. The contours in each panel denote the region containing 65, 95, 97 and 99% of the total number of classified cells. The lower panels show the corresponding cross power spectra.

is automatically determined through a Markov Chain Monte Carlo rejection sampling algorithm. The kernel purpose is meant to reproduce the power spectrum of the reference one. However, depending on the bias model a higher or lower accuracy is achieved. But the (reduced) three-point statistics corresponding to the halo realisation produced by BAM is only constrained by the chosen bias model. Therefore, we focus on this statistics to study the different bias models listed above. Some crucial improvements in the treatment of the variables, which allow us to use a low number of bins to accurately describe them are presented in Sinigaglia et al. (2021). We initially use in all our runs 300 bins for the over-density  $\delta$  and 700 bins for the rest of variables, with the exception of the T-web which uses four bins for the cosmic web type and additional 200 bins for the classification of knots (see Zhao et al. 2015). We have checked for the I-web case only, that the results do not qualitatively change using a far lower resolution of bins of  $\{200, 100, 100\}$ . An investigation of potential overfitting is presented in Sinigaglia et al. (2021). An investigation of how to use multiple reference simulations -thereby effectively increasing the reference volume- to produce accurate covariance matrices is presented in a forthcoming publication (Balaguera-Antolín et al., in prep.).

## 4.2 Halo bias calculations with invariants

A bias model including the non-linear dependence on  $\delta$ ,  $I_4$ , and  $I_5$  includes all the terms in the first row of Eq. (16) up to third order, with the exception of the term involving  $\delta s^2$  and  $s^3$  (as it does not include  $I_3$ ). This accounts for the second order anisotropic clustering. The bias contours and the cross-power spectra between the halo field, the invariants and the eigenvalues are shown in Figs. 1 and Fig. 2, respectively. The fractional and relative anisotropy (FA and RA, respectively), commonly used quantities in medical imaging (see e.g. Rajagopalan et al. 2017), are related to  $\alpha$ : FA =  $\sqrt{3}/2 (\sum_i (\lambda_i - \mu_1)^2) / I_4 = \sqrt{3} \mu_2 / (2I_4) = \sqrt{3} \alpha / I_4$  and RA =  $\sqrt{1/6} \mu_2 / \mu_1^2 = \sqrt{3} \alpha / I_1$ . The latter being similar to the halo-centric anisotropy (Ramakrishnan et al. 2019):  $\alpha' \equiv \sqrt{\alpha} / (1 + \delta)$ . From the main invariant  $I_5$  we see that the term  $I_1 I_2$  is fully specified, if in addition to  $I_5$  and  $I_1$  (through  $\delta$ ), the third principal invariant  $I_3$  is specified (see Eq. (17)). On the other hand, from the definition of  $I_4$ , we can see that  $I_4$  and  $I_1^2$  (through  $\delta$ ) generate  $I_2$ . Reversing the argument, by specifying  $\delta$  and  $I_2$  we automatically fix  $I_4$ . In this way, by describing the non-linear relation between the halo density and  $\{\delta(I_1), I_2, I_3, I_4, I_5\}$  (of which  $I_4$  is redundant), all the terms from the non-linear local and non-local density bias relation  $F_{\delta\text{NL}}(\delta)$  up to (at least) third order are



fully specified. In fact, even the common anisotropic functional dependencies are described with the invariants. Since specifying  $\{\delta, I_2, I_3, I_5\}$  corresponds to four equations involving three eigenvalues (see Eq. (17)), each eigenvalue is constrained. In this way, the ellipticity  $e$  and the prolateness  $p$ , as defined in Sect. 2.1, are fixed. In fact, it is clear now, that  $e$  and  $p$  involve the invariants  $I_1$ ,  $I_2$ , and  $I_3$ , corresponding thus to non-local bias terms which are not complete at third order in Eq. (17), since they do not involve  $I_5$ .

We conclude that the invariants  $\{I_1, I_2, I_3, I_4, I_5\}$  generate the following terms in the halo bias relation to third order (Eq. 16):  $\delta, \delta^2, \delta^3, s^2(\alpha), s^3, \delta s^2, e, p$ .

The invariant  $I_4$  is generated by  $I_1^2$  and  $I_2$ . Hence, a method able to make combinations of the type described by Eq. (18) requires only  $I_1$  and  $I_2$  to automatically also include  $I_4$ .  $I_5$  on the other hand requires  $I_1^3$ ,  $I_3$ , and  $I_1 I_2$ . We need thus to include  $I_3$  together with  $I_1 I_2$ , which is also required to model  $\delta s^2$  by  $I_1 I_4 = I_1^3 - 2I_1 I_2$ .

Then the set of variables  $\{I_1, I_2, I_3, I_1 I_2\}$  is equivalent to  $\{I_1, I_2, I_3, I_4, I_5\}$ . In terms of the statistical moments of the eigenvalues the set  $\{I_1, I_2, I_3, I_1 I_2\}$  determines  $\{I_1, \alpha, \beta\}$ , and hence, all moments to third order  $\{\mu_1, \mu_2, \mu_3\}$ .

We can also replicate the invariants  $I_i$  with the eigenvalues. A first naive attempt consists of using a model such as  $\{I_1, \lambda_1, \lambda_2, \lambda_3\}$ . This however, will not include terms like  $\lambda_i \lambda_j$ , nor  $\lambda_i^2 \lambda_j$  with  $i \neq j$ . This implies that terms such as  $I_2, I_3, I_1 I_2$  cannot be constructed. It is tempting to construct combined variables such as  $\lambda_{ij} = \lambda_i + \lambda_j$  with  $i \neq j$  to account for those mixed terms. However, according to Eq. (18) by doing so we would have the same weights for terms which require an independent treatment to construct the various bias terms. One could further extend this model including  $I_1 I_2$ , however at the computational expense of having five variables instead of four to describe all relevant bias terms up to third order neglecting velocity and short range non-local terms. Nonetheless, the model  $\{I_1, \lambda_1, \lambda_2, \lambda_3\}$  constrains powers of  $\delta$ , and  $\{I_4, I_5, e, p\}$ . It is thus an interesting model to test the capability of BAM to combine different variables to effectively treat a series of bias terms.

For computational reasons, it is also interesting to consider the case of  $\{\delta, I_2, I_3\}$  (hereafter dubbed I-web or I-web-V when based on the tidal field or velocity shear tensor, respectively), as compared to the complete invariants set. As shown above, the  $I_1 I_2$  is well modelled through  $I_3$ , and hence similar results are expected from including it or not.

In fact, one needs to realise that  $I_1 I_2$  is related to  $I_3$  through the equation:

$$I_1 I_2 = 3I_3 + \sum_{i \neq j} \lambda_i \lambda_j^2. \quad (19)$$

From this we see that when all three eigenvalues are similar  $I_1 I_2 \simeq 9I_3$ , implying an isotropic collapse or expansion, which can happen for cosmic web types such as knots or voids. Moreover, when two eigenvalues are close to each other  $\lambda_1 \simeq \lambda_2$  (the same argument is valid for  $\lambda_2 \simeq \lambda_3$ ) we have  $I_1 I_2 \simeq 3I_3 + 2(\lambda_1^3 + \lambda_1^2 \lambda_3 + \lambda_1 \lambda_3^2)$  and  $I_3 \simeq \lambda_1^2 \lambda_3$ . If we further demand all terms to be proportional to  $I_3$ , then  $I_1 I_2 \simeq (3 + 2c)I_3$  with  $c$  being a constant factor, which is fulfilled when  $\lambda_1^3 + \lambda_1^2 \lambda_3 + \lambda_1 \lambda_3^2 \simeq c \lambda_1^2 \lambda_3$ . This yields a quadratic equation for  $\lambda_3$ :  $\lambda_3^2 + (1 - c)\lambda_1 \lambda_3 + \lambda_1^2 \simeq 0$ . Hence,  $\lambda_3 \simeq -\lambda_1[1 - c \pm \sqrt{(1 - c)^2 - 4}]/2$ , which for the particular case of  $c = -1$  reduces to  $\lambda_3 \simeq -\lambda_1$ . This is the typical sit-

uation of a filament or sheet for which two eigenvalues are similar sharing the same sign, and the third one has opposite sign. A whole family of valid solutions is given for  $c < -1$ , which does not force the third eigenvalue to have the same absolute value as the other two. It is especially when the three eigenvalues are different, that the  $I_1 I_2$  term adds information, and will need to be investigated further in future work.

Our study investigates the major contributions up to third order in the halo bias expansion, as they dominate the statistics within the scales we are considering in this work. It is important to stress, however, that BAM does not restrict the dependencies in the variables (generating functions) to any truncated order.

The total number of models considered in this study are summarised as follows:

- Local DM  $\delta$ :  $\{\delta\}$ ,
- $\delta$ +T-web:  $\{\delta, t_{\text{cw}}=\{\text{knot, filament, sheet, void}\} \sim \{\delta(I_1), \tilde{s}^2(\tilde{\alpha}), \tilde{s}^3, \tilde{e}, \tilde{p}\}$ ,
- PT-web-q:  $\{\delta, I_4\}$ ,
- PT-web-qa:  $\{\delta, I_4, s^2(\alpha)\} \sim \{\delta, I_2, I_4\}$ ,
- PT-web:  $\{\delta, I_4, I_5\}$ ,
- $\lambda$ -web:  $\{\delta, \lambda_1, \lambda_2, \lambda_3\} \sim \{\delta, I_4, I_5, e, p\}$ ,
- I-web:  $\{\delta, I_2, I_3\} \sim \{\delta, s^2(\alpha), \tilde{s}^3, \tilde{\delta s}^2, e, p\}$ ,
- I-web-c:  $\{\delta, I_2, I_3, I_1 I_2\} \sim \{\delta, I_2, I_3, I_4, I_5\} \sim \{\delta, s^2(\alpha), s^3, \delta s^2, e, p\}$ ,

with  $\tilde{x}$  indicating restricted information on  $x$ . As explained in appendix A the T-web has only partial information of the whole parameter space spanned by the invariants (I-web). There is a crucial difference between the T-web and the I-web models, which lies in the binning of the variables given by the invariants or the eigenvalues, the same way the density field is binned. The T-web is not only solely based on the invariants  $I_1, I_2, I_3$ , but also restricts the information to a particular cosmic web type, and hence corresponds to only four additional bins to the ones used for the density.

The plots representing the relation between the invariants and the halo density field (such as Figs. 1 or 2) show how BAM captures the full non-linear and stochastic relation between each variable and the halo realisation from the reference simulation. This is accurately demonstrated in (Pellejero-Ibañez et al. 2020). In that work halo populations down to  $\gtrsim 10^8 h^{-1} M_\odot$  were studied. In that case, the halo population has a very low bias, and in consequence, its two- and three-point statistics are closer to the dark matter field. Hence, simpler bias models, such as  $\delta$ +T-web succeed to reproduce the summary statistics. However, the non-linear local dark matter density dependence becomes very complex, having an increasing range of halo number counts towards higher mass resolutions, and simple power law bias models are shown to fail. The study presented in this work, can be thus particularly important for intermediate halo masses, hosting emission line galaxies.

The invariants of the velocity shear tensor (instead of the tidal field tensor) can be used in the analysis yielding an effective description of further bias terms in Eq. 16 (see §5.1.1).

## 5 ANALYSIS OF GRAVITY CALCULATIONS

In this section, we present the results after applying the

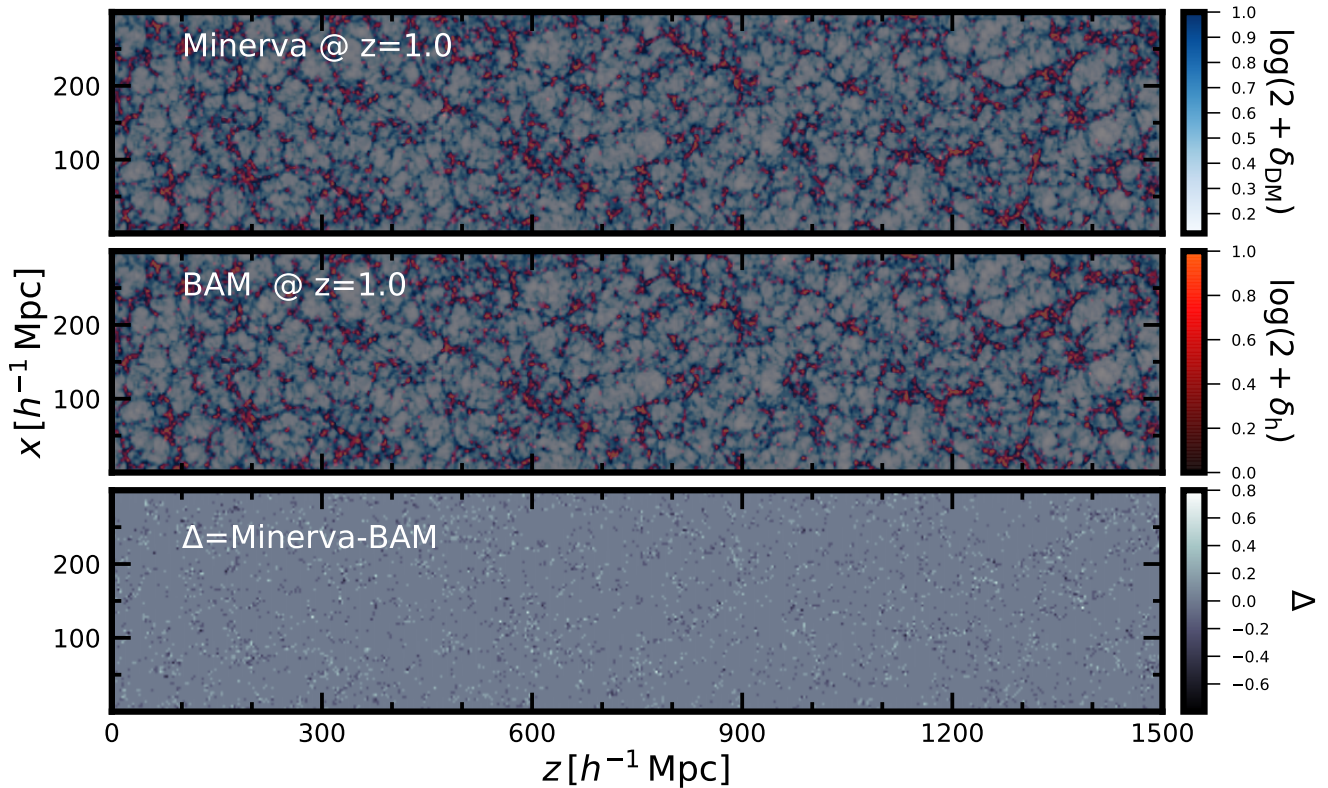


**Figure 3.** Slices through the simulated cosmic volumes. Top panels: halo over-density field  $\delta_h$  (red colour range) vs  $N$ -body dark matter field  $\delta$  (blue colour range), top panel: from the  $N$ -body catalogue (4500 CPU hrs), middle panel: from the BAM mock with the I-web model (0.042 CPU hrs without velocities). Bottom panel: difference between the two halo fields.

Bias Assignment Method (BAM code: Balaguera-Antolínez et al. 2019, 2020; Pellejero-Ibañez et al. 2020, and §4), which relates the halo number counts per cell in a mesh ( $3 h^{-1}$  Mpc cell side resolution in a  $1.5 h^{-1}$  Gpc cubical volume) to a number of dependencies given by Eq. (13).

We focus in this work on the following biasing models: local  $\delta$ ;  $\delta$ +T-web:  $\{\delta, t_{cw}\}$ ; PT-web-q:  $\{\delta, I_4\}$ ; PT-web:  $\{\delta, I_4, I_5\}$ ; and I-web:  $\{\delta, I_2, I_3\}$ . The invariants and their relation to the halo number over-density  $\delta_h$  are shown in Fig. 1. The bias relation and the cross power spectra of  $I_3$  and  $I_1 I_2$  turn out to have a relatively similar grained structure, similar cross power spectra, and bias relations. In fact,  $I_1 I_2$  is proportional to  $I_3$  for knots and voids, when the three eigenvalues are close to each other, and for filaments and sheets when two eigenvalues are roughly the same (see §2.1). Hence, we can save in this study the cross term, reaching equal accuracy. It becomes visually clear how  $I_1$  and  $I_2$  can build  $I_4$  (with a  $\delta^2$  term yields  $s^2$ ), and how  $I_1, I_3$  (and  $I_1 I_2$ ) can generate  $I_5$  (with a  $\delta^3$  term yields  $s^3$ ). The results from BAM are summarised in Figs. 4–9.

Several previous works have detected non-local bias in  $N$ -body simulations by doing truncated bias expansion (for quadratic terms see Chan et al. 2012; Baldauf et al. 2012) and (for cubic terms see Modi et al. 2017; Abidi & Baldauf 2018). We note, that in the present work we manage to confirm such dependencies by reproducing the three-dimensional halo distribution including the phases at small scales, as il-

lustrated in Fig. 3. The two halo distributions from the full gravity calculation and the BAM mock using the I-web look very similar. Their tiny differences are a consequence of accounting for the full stochastic nature of the halo bias relation at the cell resolution (see Eq. 13). This is particularly useful, as it permits us to produce accurate synthetic halo catalogues without having to make the expensive computations of  $N$ -body codes. The BAM-code is especially efficient (see computing requirements of the PATCHY code, which are comparable to BAM in contrast to other methods in Blot et al. (2019) and Pellejero-Ibañez et al. (2020)).

### 5.1 Two- and three-point statistics analysis

We analyse both the two- and three-point statistics for different models using first a single reference catalogue, and second a set of ten reference catalogues.

We are using in this work consistently the same initial conditions at scales larger than the cell size resolution with BAM realisations as in the corresponding reference simulation. This already reduces to a great extent the effect of cosmic variance when making a comparison among them. Nonetheless, we have seen that the lowest few modes in the power spectrum are still affected by cosmic variance through halo bias.

Using only one reference simulation enables us to investigate the accuracy in reproducing the statistics of that particular realisation. However, we extend the study to ten refer-

ence simulations, as this provides insights on the robustness of the method against different realisations.

The power spectra corresponding to different BAM runs w.r.t. one reference catalogue are shown in Fig. 4. We have shown that we can reach with all the considered models an accuracy within 2% in each mode, yielding residuals<sup>1</sup> below 1%. The results considering different realisations yield compatible power spectra for the various cosmic web classification methods (see Fig. 5). In particular, we show results after the method is well converged with the local  $\delta$ , the  $\delta$ +T-web, the I-web, and the I-web-V model. The same level of accuracy is achieved for the PT-web, PT-web-q, and  $\lambda$ -web models in terms of the two-point statistics. We need to go to higher order statistics to find differences.

The three-point statistics is commonly used to constrain the bias (see e.g. Matarrese et al. 1997; Sefusatti & Komatsu 2007; Baldauf et al. 2012; Pollack et al. 2012; Saito et al. 2014; Kitaura et al. 2015; Angulo et al. 2015b; Baldauf et al. 2015; Angulo et al. 2015a; Gil-Marín et al. 2017).

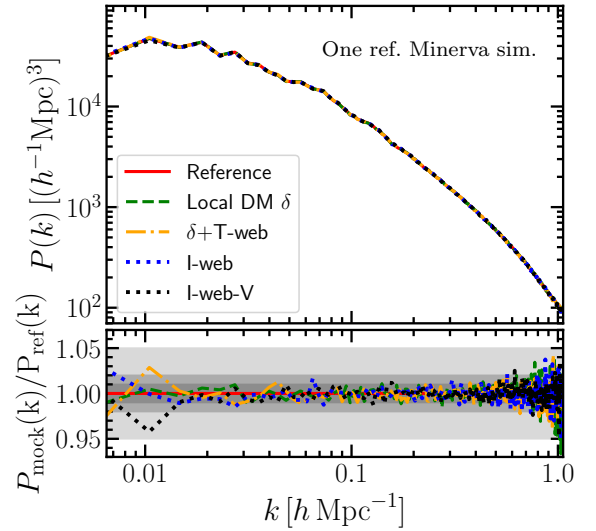
It is investigated here in Fourier space through the reduced bi-spectrum  $Q(\theta_{12})$  as a function of the normalised angle  $\theta_{12}$  between the  $\vec{k}$ -vectors  $\vec{k}_1$  and  $\vec{k}_2$  (see Figs. 6–9). Comparing BAM runs with only local density information vs I-web, we find evidence for non-local bias at the  $4.8\sigma$  confidence level (an information gain of  $\sim 3.4\sigma$  over  $\delta$ +T-web), being very conservative (see §5.2). One should note that this confidence level is based on the assumption of different seed perturbations, and hence it carries an overestimation of uncertainty due to cosmic variance. Accordingly, the statistical significance of a non-local bias detection is expected to be stronger using more accurate covariance matrices with smaller uncertainties corresponding to the same initial conditions.

In particular, we consider triangle configurations in Fourier space constrained by the following two sides:  $|\vec{k}_1| = 0.02, 0.05, 0.1 h \text{ Mpc}^{-1}$  &  $|\vec{k}_2| = |\vec{k}_1|$ ; and  $|\vec{k}_1| = 0.1 h \text{ Mpc}^{-1}$  &  $|\vec{k}_2| = 2|\vec{k}_1|$ , as a function of the  $\theta_{12}$  angle.

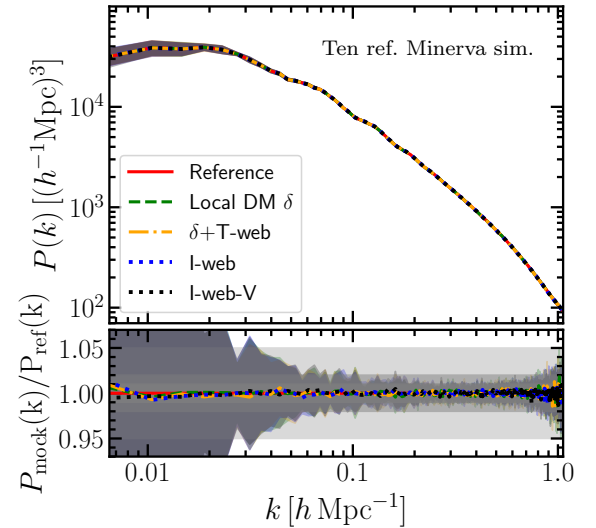
The bi-spectra at the largest scales are all compatible with each other within error bars (configuration corresponding to  $|\vec{k}_1| = 0.02$  &  $|\vec{k}_2| = |\vec{k}_1|$ , on the left in Fig. 6). It is remarkable, that already at large scales with configurations of  $|\vec{k}_1| = 0.05 h \text{ Mpc}^{-1}$  &  $|\vec{k}_2| = |\vec{k}_1|$  non-negligible differences can be found, as we further analyze below. These differences increase towards smaller scales (see right panels). We stop at the configuration of  $|\vec{k}_1| = 0.1 h \text{ Mpc}^{-1}$  &  $|\vec{k}_2| = 2|\vec{k}_1|$ , since this is the typically shown one, as being relevant to BAO and RSD analysis. Also higher  $k$  configurations become computationally more expensive, and we plan to extend this work including velocity and short range non-local bias terms, for which smaller scales become interesting.

Fig. 7 shows the comparison between I-web vs I-web-c, PT-web vs  $\lambda$ -web, and PT-web vs PT-web-qa. The left panel shows the similarity from considering or neglecting the cross term  $I_1 I_2$ . As we argued before,  $I_1 I_2$  is well represented by  $I_3$ , which effectively includes the third order non-local bias terms  $\delta s^2$  and  $s^3$ . From this we conclude that we can save in general the usage of an additional field. Although further analysis towards small scales will have to investigate this. The

<sup>1</sup> Defined as the sum of the absolute difference between the reference and the BAM catalogue’s power spectra in the whole  $k$ -mode range up to 70% of the Nyquist frequency.



**Figure 4.** Halo power spectra from one reference Minerva simulation in red, and from BAM realisations with bias models given by  $\delta$ -,  $\delta$ +T-, and I-web using the same initial conditions (ICs). On the bottom panel corresponding ratios w.r.t. the reference are shown. The different shaded areas stand for 1, 2, and 5% error bars. See §4.2 for PT-web and PT-web-q.



**Figure 5.** Same as Fig. 4 but based on ten reference Minerva simulations with different seed perturbations in the initial conditions showing the corresponding mean and  $1\text{-}\sigma$  contours for each case (they overlap significantly).

middle panel confirms that BAM is actually solving Eq. (18), as very different generating functions, which are supposed to approximately coincide in the final bias terms they produce, do actually have very similar power spectra and bi-spectra. The role of ellipticity and prolateness seems to be moderate in this statistics at those large scales. However, the difference between  $I_4$  and  $\alpha$  is complementary, adding more information on anisotropic clustering at second order. This is demonstrated in the additional test shown in the right panel, which also partially explains the difference between the PT-web and the I-web models, and further analysed below. In

One ref. Minerva sim.

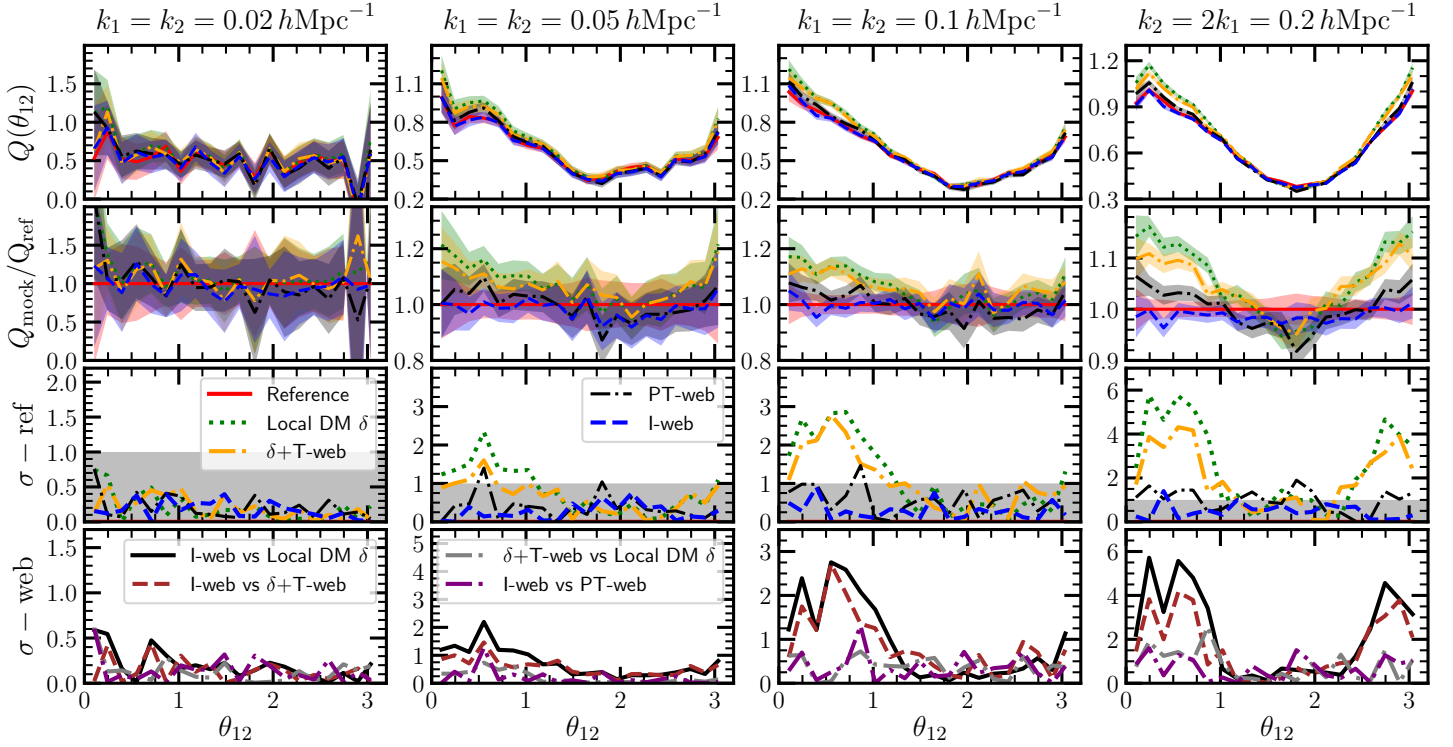


**Figure 6.** Reduced bi-spectra of the reference  $N$ -body halo catalogue (red solid) and the BAM mocks with the bias relation including: only  $\delta$  (green dotted),  $\delta$ +T-web (dot-dashed orange), PT-web:  $\{\delta, I_4, I_5\}$ , and the I-web  $\{\delta, I_2, I_3\}$ . The corresponding ratios are shown in the second row. The third row shows the sigma difference:  $\sigma_{\text{ref}}(X\text{-web}) = |Q_{X\text{-web}} - Q_{\text{ref}}|/(\sqrt{2}\sigma)$ , with  $\sigma$  being the standard deviation extracted from the 300 Minerva catalogues. The last row shows the difference between two X and Y BAM mocks  $\sigma_{\text{web}}(X, Y) = |\sigma_{\text{ref}}(X\text{-web}) - \sigma_{\text{ref}}(Y\text{-web})|$ , as indicated in the legend. The largest evidence for non-local bias is found for the I-web:  $\sigma_{\text{web}}(\text{I-web}, \delta)$ . This is a very conservative estimate, since the halo realisations share the same underlying dark matter field above a resolution of  $3 h^{-1}$  Mpc.

One ref. Minerva sim.

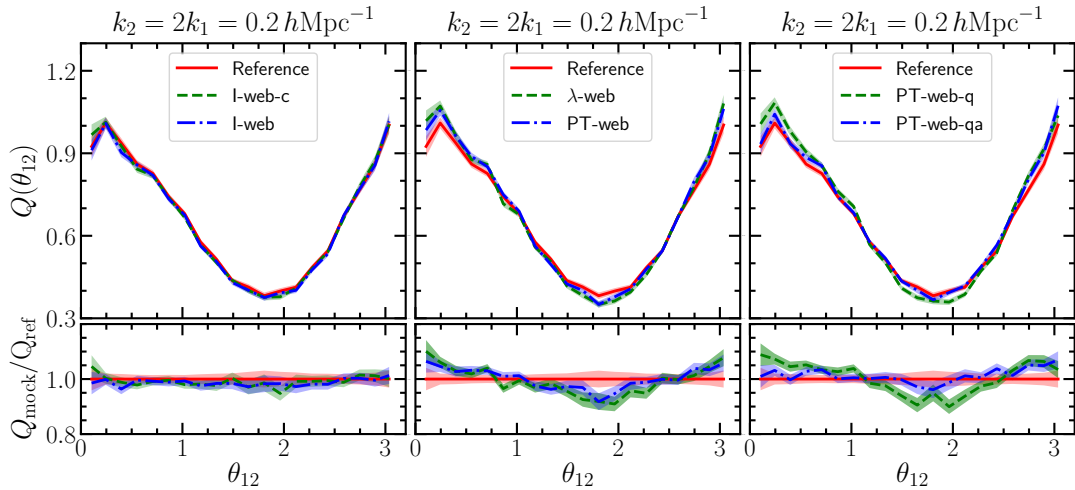


**Figure 7.** Reduced bi-spectra of one reference  $N$ -body halo catalogue (red solid) and the BAM mocks with the bias relation including on the left: the I-web-c:  $\{\delta, I_2, I_3, I_1 I_2\}$  (green dashed) and the I-web:  $\{\delta, I_2, I_3\}$  (blue dash-dotted); in the middle:  $\lambda$ -web:  $\{\lambda_1, \lambda_2, \lambda_3\}$  and PT-web:  $\{\delta, I_4, I_5\}$ ; and on the right: PT-web-q:  $\{\delta, I_4\}$  vs PT-web-qa:  $\{\delta, I_4, s^2(\alpha)\}$  (with  $1\text{-}\sigma$  contours from the 300 Minerva reference catalogues).

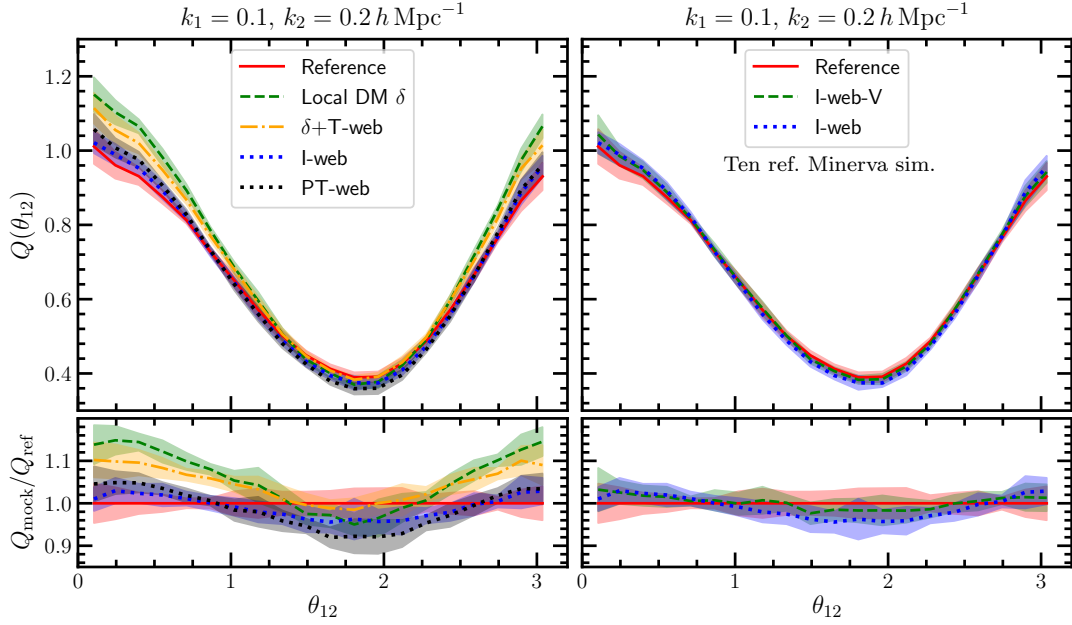


**Figure 8.** Left panel: comparison between the bi-spectra corresponding to ten Minerva simulations and  $\delta$ ,  $\delta$ +T-web, PT-web and I-web calculations (analogous to Fig. 7, including  $1\text{-}\sigma$  contours from ten realisations for each case). Right panel: the same as left panel showing I-web vs. I-web-V.

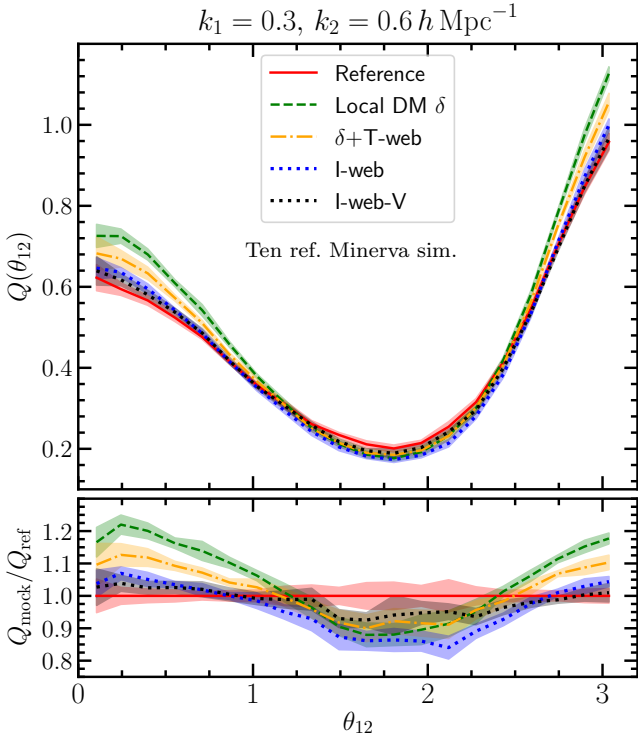


**Figure 9.** Same as Fig. 8 at a smaller scale configuration.

the latter comparison the third order cross term  $\delta s^2$ , i.e., a further specification on the third order anisotropic clustering, can also play a role. It is tempting to expect BAM according to Eq. (18) to be able to construct  $s^2(\alpha)$  from knowing  $\delta$  and  $I_4$ , since  $s^2 = I_4 - \delta^2/3$ . However, a greater accuracy is achieved when explicitly providing  $s^2$  due to the low number of bins used. Adding a redundant variable in this case

effectively increases the number of bins and provides more accurate results. We get bi-spectra, which are significantly closer to the reference (compare the  $-\text{PT-web-q-}$  green to the  $-\text{PT-web-qa-}$  blue dashed-dotted line on the right panel of Fig. 7).

We notice that  $\lambda$ -web does not fully characterise  $s^3$  since  $I_5$  needs an additional  $I_3$  term which is not included in this model.

We compute the standard deviation w.r.t. the reference simulation as:  $\sigma_{\text{ref}}(\text{X-web}) \equiv |Q_{\text{X-web}} - Q_{\text{ref}}|/(\sqrt{2}\sigma)$ , where we have calculated the covariance matrices of the bi-spectra from the reference simulation, and assume the same derived  $\sigma$  error bars apply for the BAM realisations based on our previous experience (Balaguera-Antolínez et al. 2020). Since the theoretical model in this case has a comparable error bar to the different models, we adopt a conservative procedure to estimate the significance of our measurements. In particular, we define the tidal field based non-local bias detection with the various X-web models, as  $\sigma_{\mathcal{T}}(\text{X-web}) \equiv \sigma(\text{X-web}) - \sigma(\delta\text{-web})$ . The information gain of the I-web w.r.t. the T-web is expressed via  $\sigma(\text{I-web, T-web}) = \sigma(\text{I-web}) - \sigma(\text{T-web})$ . The significances  $\sigma_{\mathcal{T}}(\text{X-web})$  and  $\sigma(\text{I-web, T-web})$  shown in the lower panels of Fig. 6 are positive, indicating that there is a detection of non-local bias and an information gain. By averaging over the angle range, which shows most differences ( $0.25 < \theta_{12} < 0.75$ ), we find  $\sigma_{\mathcal{T}}(\text{I-web}) = 4.8\sigma$ ,  $\sigma_{\mathcal{T}}(\text{T-web}) = 1.4\sigma$ , and hence  $\sigma_{\text{web}}(\text{I-web, T-web}) = 3.4\sigma$ .

This implies that we have a clear detection of the non-local bias in the bi-spectrum with the I-web, and a considerable information gain w.r.t the T-web.

### 5.1.1 The cosmic web based on the velocity shear tensor

In this section, we present calculations with BAM using the I-web based on the velocity shear instead of the tidal field

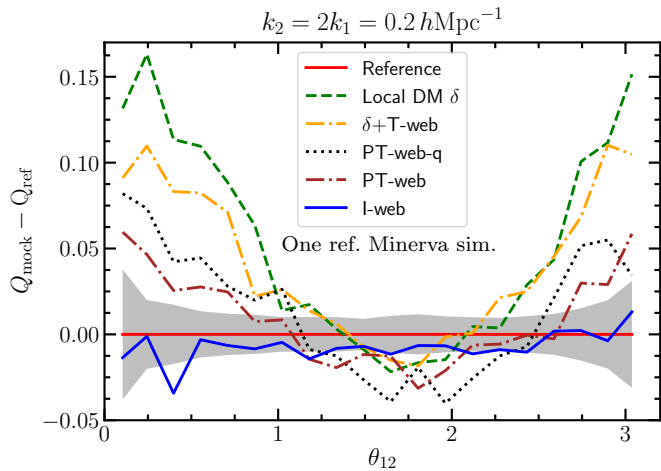


**Figure 10.** Difference of reduced bi-spectra of the reference  $N$ -body halo catalogue (red solid) and the BAM mocks with the bias relation including: only  $\delta$  (green dotted),  $\delta$ +T-web (dashed-dotted yellow), I-web:  $\{\delta, I_2, I_3\}$ , PT-web:  $\{\delta, I_4, I_5\}$ , and PT-web-q:  $\{\delta, I_4\}$ . The grey area corresponds to the standard deviation from computing the bi-spectra for 300 Minerva simulations.

tensor, i.e. the I-web-V model. The velocity field is taken from the Minerva reference simulation using a nearest-grid-point mass assignment scheme to define it on the same mesh as the density field. This model will effectively include not only terms in the first row of Eq. (16) but also terms in the second row for which  $\theta \neq \delta$ .

In particular, we consider the following variables for BAM based on the I-web-V:  $\{\delta, I_1(\mathbf{v}), I_2(\mathbf{v}), I_3(\mathbf{v})\}$  with a binning of  $\{200, 100, 100, 70\}$ . This is comparable to the one of the I-web based on the tidal field tensor.

In fact, we find very similar bi-spectra which are not strongly affected by cosmic variance for the considered configurations (see left panel in Fig. 8).

A more careful analysis, comparing with velocity shear based realisations hints towards a slightly higher precision when relying on the I-web-V (see right panel in Fig. 8).

Since the results relying on the tidal field were already compatible with the reference simulation in the power spectrum and in the considered bi-spectrum configurations for the I-web case, we extend the three point statistics analysis to smaller scales.

Fig. 9 shows that the additional information contained in the velocity field can provide a more precise bias description. In particular, the bi-spectra considering configurations of  $k_2 = 2k_1 \sim 0.6 h \text{ Mpc}^{-1}$  are, in general, compatible within  $1\text{-}\sigma$  with the reference simulation when considering the velocity shear, as opposed to considering only the tidal field tensor. Still, some slight discrepancy between the reference bi-spectrum and the I-web-V BAM realisations can be found. This could potentially be improved with an adequate binning or maybe relying on a larger number of reference simulations. Further investigation on this is left for future work.

## 5.2 Statistical significance of the bias models

To compute the statistical significance of the different models we rely on the  $\chi^2$  statistics (see Fig. 10).

We assume that the bi-spectrum error bars are given by the

set of 300 Minerva simulations. We should note, that the real error bars must be somewhat lower, since the cosmic variance is suppressed to some extent by using the same initial conditions at a down-sampled resolution.

In Tab. 1 we show individual measurements of  $\chi^2/\text{dof}$  (number of degrees of freedom, the amount of  $\theta_{12}$  bins in our case) and its interpretation from the frequentist point of view. We show what is the probability of finding a sample of the  $\chi^2$  distribution  $X$  greater than the one given by the mocks  $P(X > \chi^2)$ . We assume that the computed  $\chi^2$  is not drawn from the same distribution, if its probability is not within the 99% of the distribution. We found that the only mock satisfying this condition was the one produced in the I-web case.

In Tab. 2 we show the comparison between  $\chi^2/\text{dof}$ , and the interpretation in terms of Bayes factors. Since we assume that both the priors and the probability of the data (also called the evidence) are the same in all of the cases, the Bayes factor reduces to the likelihood ratio. The grades of evidence are taken from Jeffreys (1939). We find that for the largest scales there is no evidence for preferring any model over another. However, towards smaller scales the I-web parametrisation evidence increases, as compared to any other model. The I-web shows a clear preference w.r.t. the local density and the  $\delta$ +T-web models already for the configuration  $k_1 = k_2 = 0.1 h \text{ Mpc}^{-1}$ . The PT-web and PT-web-q models compete with the I-web until the  $k_1 = 0.1$  &  $k_2 = 0.2 h \text{ Mpc}^{-1}$  configuration is achieved, for which we find evidence that the I-web is required to fit the  $N$ -body reference halo catalogue.

From this analysis, we infer that the I-web runs are the only ones, which are indistinguishable from the reference (at the considered scales). We also find that the PT-web model does not match the reference simulation, but performs better than the PT-web-q model, which contains only up to quadratic terms. This study implies that we have a considerable gain from including second order non-local bias ( $I_4$ ) terms (black dotted vs green dashed lines, and an additional more moderate information gain from including third order non-local bias ( $I_5$ ) terms (see brown dashed-dotted vs black dotted lines in Fig. 6). A considerable information gain is obtained from using the I-web, which has a more accurate description of the anisotropic clustering as discussed above (see blue solid vs brown dashed-dotted lines in Fig. 6).

## 6 DISCUSSION AND CONCLUSIONS

In this work we have investigated the characterisation of the gravitational deformation tensor through its invariants and its impact on the distribution of dark matter tracers. We have shown how to link the latter with the usual characterisation of the cosmic web relying on combinations of the eigenvalues and their connection to the perturbative halo bias expansion (see, e.g., Bardeen et al. 1986; Sheth & Tormen 2002; McDonald & Roy 2009; Chan et al. 2012; Pollack et al. 2012; Baldauf et al. 2012; Pollack et al. 2014; Saito et al. 2014; Modi et al. 2017; Abidi & Baldauf 2018; Lazeyras & Schmidt 2018; Eggemeier et al. 2021). We have done this along the lines of Schmittfull et al. (2019), populating the dark matter field at the Eulerian field level. This has enabled us to reproduce the results of full gravity calculations based on  $N$ -body simulations to unprecedented accuracy in

Bias model	Bi-spectrum configuration											
	$k_1 = k_2 = 0.02$			$k_1 = k_2 = 0.05$			$k_1 = k_2 = 0.1$			$k_1 = 0.1 \& k_2 = 0.2$		
	$\chi^2$	$P(X > \chi^2)$	MR	$\chi^2$	$P(X > \chi^2)$	MR	$\chi^2$	$P(X > \chi^2)$	MR	$\chi^2$	$P(X > \chi^2)$	MR
Local DM $\delta$	0.17	99%	N	2.0	0.4%	Y	4.5	$\sim 0\%$	Y	20.2	$\sim 0\%$	Y
$\delta$ +T-web	0.13	99%	N	1.14	29.4%	N	3.37	$\sim 0\%$	Y	11.7	$\sim 0\%$	Y
PT-web-q	0.15	99%	N	0.61	90%	N	1.13	30%	N	6.16	$\sim 0\%$	Y
PT-web	0.2	99%	N	0.5	96%	N	0.9	58%	N	2.5	$\sim 0\%$	Y
I-web	0.1	99%	N	0.2	99%	N	0.3	99%	N	0.7	85%	N

**Table 1.** Individual statistics for the different bias models on the corresponding bi-spectra: the  $\chi^2$ , the probability of a sampled  $X$  being greater than the measured  $\chi^2$  and the model rejection MR {N: No, Y: Yes}. We assume a model can be rejected when the measured  $\chi^2$  is further than the 99% probability of being within the  $\chi^2_{\text{dof}}$  distribution (dof is the number of degrees of freedom, number of bins in our case). The cell color gray indicates that the model is rejected w.r.t. the reference, while light gray means that it cannot be rejected, with the I-web being the only model remaining green throughout all considered configurations.

Bias models	Bi-spectrum configuration											
	$k_1 = k_2 = 0.02$			$k_1 = k_2 = 0.05$			$k_1 = k_2 = 0.1$			$k_1 = 0.1 \& k_2 = 0.2$		
	$\Delta\chi^2$	BF	E	$\Delta\chi^2$	BF	E	$\Delta\chi^2$	BF	E	$\Delta\chi^2$	BF	E
I-web vs local DM $\delta$	0.08	1.04	N	1.81	2.47	N	4.21	8.21	Y1	19.5	17402	Y4
I-web vs $\delta$ +T-web	0.04	1.02	N	0.94	1.60	N	3.1	4.72	Y1	11.06	252	Y4
I-web vs PT-web-q	0.06	1.03	N	0.41	1.23	N	0.87	1.54	N	5.48	15.47	Y3
I-web vs PT-web	0.06	1.03	N	0.30	1.16	N	0.64	1.37	N	1.81	2.50	Y1

**Table 2.** Comparison of bias models based on the corresponding bi-spectra, showing the differences  $\Delta\chi^2$ , the corresponding Bayes factors BF, and the evidence grades of the difference in the models: {N: No evidence, Y1: Substantial, Y2: Strong, Y3: Very Strong, Y4: Decisive}. The evidence grades are taken from [Jeffreys \(1939\)](#). The cell color light gray means that there is no evidence that a model is preferred over the I-web model, while gray stands for evidence against the various models w.r.t. the I-web model. All cases become red, meaning that all models are disfavoured w.r.t. the I-web.

the two- and three-point statistics of dark matter tracers. To this end we have relied on the Bias Assignment Method (BAM [Balaguera-Antolínez et al. 2019, 2020](#); [Pellejero-Ibañez et al. 2020](#)), which acts as a physically motivated supervised machine learning method able to combine generating functions to produce halo counts on a regular mesh. This approach has been followed by similar concepts relying on deep learning. While they are very promising (see e.g., [Zhang et al. 2019](#)) when trying to reproduce the summary statistics on large cosmic volumes, they do still not reach the precision of the BAM algorithm ([Kodi Ramanah et al. 2019](#)). Machine learning methods are not only more difficult to interpret in terms of physical insights, but also very sensitive to the definition of the cost function they aim at minimising, and other set-up parameters like the number of layers, etc. Hereby, the non-local dependencies are difficult to track. Physical models help to increase the accuracy, as demonstrated by combining the Zel'dovich approximation with machine learning ([He et al. 2019](#)). The BAM approach aims in fact at providing the maximum physical information to minimize the uncertainties encoded in a single kernel (as a function of  $k$  in Fourier space), which is extracted within a Markov Chain Monte Carlo rejection algorithm, learning from the reference simulation. Hence, deep learning approaches could benefit from the insights provided in this work.

The bi-spectrum analysis shows that already at configurations of  $k_1 = k_2 = 0.05 h \text{ Mpc}^{-1}$  the invariants become necessary. This accuracy increases when using the invariants of the tidal shear tensor towards smaller scales as expected from having a more complete anisotropic bias description.

A precise description of anisotropic clustering has turned out to be crucial on large scales confirming its importance found in previous work ([Ramakrishnan et al. 2019](#)).

In summary, we have succeeded to find a consistent picture

at scales relevant to BAO and RSD analysis. In forthcoming publications, the connection to the galaxy distribution, redshift space distortions, and covariance matrices going down to lower halo masses will be presented ([Balaguera-Antolínez, Kitaura et al in prep.](#)). From recent studies showing that an accurate fit to the two- and three-point statistics implies accurate covariance matrices ([Baumgarten & Chuang 2018](#)), we expect that the corresponding four-point statistics will also be well reproduced with BAM relying on the I-web. In fact, previous versions of the BAM code using the T-web already reproduced well the covariance matrices from  $N$ -body simulations using the information of the power spectra up to  $k = 0.2 h \text{ Mpc}^{-1}$  ([Balaguera-Antolínez et al. 2020](#)).

These findings suggest that one might find very complete galaxy bias descriptions based on a few terms constructed with invariants of the tidal field or velocity shear tensor. In particular, one could easily extend the bias model suggested by ([Fry & Gaztanaga 1993](#); [Cen & Ostriker 1993](#); [Abel et al. 2012](#)) with something like:  $\rho_g \propto h(\{d_i\}) f(\sum_i a_i (c_i + g(\eta_i))^{b_i})$ , where  $f$ ,  $g$ , and  $h$  are some appropriate functions,  $a_i$ ,  $b_i$ ,  $c_i$ , and  $\{d_i\}$  are a set of bias factors, and  $\eta_i$  being, e.g.,  $\{\delta(I_1), I_2, I_3, (I_1 I_2)\}$ . The function  $h$  typically models the suppression of the appearance of galaxies towards low densities through a threshold or decaying exponential ([Kaiser 1984](#); [Kitaura et al. 2014](#); [Neyrinck et al. 2014](#)). Some interesting cases can be found for  $f$  being the identity function and  $g$  being an exponential, or reversing the roles of  $f$  and  $g$ . We leave a study of the velocity shear, vorticity, as well as density short range terms as a function of redshift for future work. This work also suggests that galaxy evolution and formation studies, which are recently relying on cosmic web classifications, could potentially benefit from a different angle. Parameter regions defined by the multidimensional space spanned by the invariants could become the

sights to look at, to identify common properties of galaxies. We have worked out, how one could associate those parameter regions to different physical properties. As an example, one could relate a particular I-web parameter region to a combination of cosmic web types with their associated probabilities. As a further application, the I-web is expected to improve the halo mass reconstruction, previously relying on the T-web (Zhao et al. 2015).

We conclude that the invariants of the gravitationally evolved tidal field tensor at Eulerian coordinates are able to characterize the cosmic web, and the halo bias terms down to the Eulerian field level to great accuracy. Thus, they could be useful to extract cosmological information from the next generation of galaxy surveys.

## DATA AVAILABILITY

The data underlying this article will be shared on reasonable request to the corresponding author.

## ACKNOWLEDGMENTS

The authors thank A. Sánchez, P. McDonald, R. Sheth, R. Angulo, R. van de Weygaert, C. Zhao, C.-H. Chuang, C. Dalla Vecchia, and J. A. Rubiño-Martín for discussions. Special thanks to AS and CDV for kindly providing the Minerva simulations, and CZ and CHC for the bispectrum code. FSK and ABA acknowledge the IAC facilities and the Spanish Ministry of Economy and Competitiveness (MINECO) under the Severo Ochoa program SEV-2015-0548, AYA2017-89891-P and CEX2019-1124000920-S grants. FSK also thanks the RYC2015-18693 grant. FS thanks the University of Padova and the IAC. MPI thanks the AYA2012-39702-C02-01 and ERC-SG 716151 (BACCO) grants.

## REFERENCES

Abel T., Hahn O., Kaehler R., 2012, *MNRAS*, **427**, 61  
 Abidi M. M., Baldauf T., 2018, *J. Cosmology Astropart. Phys.*, **2018**, 029  
 Ahn K., Iliev I. T., Shapiro P. R., Srisawat C., 2015, *MNRAS*, **450**, 1486  
 Alam S., Zu Y., Peacock J. A., Mandelbaum R., 2019, *MNRAS*, **483**, 4501  
 Amendola L., Appleby S., Avgoustidis A., others 2016, preprint, ([arXiv:1606.00180](https://arxiv.org/abs/1606.00180))  
 Angulo R. E., Baugh C. M., Lacey C. G., 2008, *MNRAS*, **387**, 921  
 Angulo R., Fasiello M., Senatore L., Vlah Z., 2015a, *J. Cosmology Astropart. Phys.*, **2015**, 029  
 Angulo R. E., Foreman S., Schmittfull M., Senatore L., 2015b, *J. Cosmology Astropart. Phys.*, **2015**, 039  
 Aragón-Calvo M. A., Jones B. J. T., Van de Weygaert R., Van der Hulst J. M., 2007a, *A&A*, **474**, 315  
 Aragón-Calvo M. A., Van de Weygaert R., Jones B. J. T., Van der Hulst J. M., 2007b, *ApJ*, **655**, L5  
 Aragón-Calvo M. A., Platen E., Van de Weygaert R., Szalay A. S., 2010, *ApJ*, **723**, 364  
 Aragón Calvo M. A., Neyrinck M. C., Silk J., 2019, *The Open Journal of Astrophysics*, **2**, 7  
 Arnold V. I., Shandarin S. F., Zeldovich I. B., 1982, *Geophysical and Astrophysical Fluid Dynamics*, **20**, 111

Assassi V., Baumann D., Green D., Zaldarriaga M., 2014, *J. Cosmology Astropart. Phys.*, **2014**, 056  
 Avila S., Murray S. G., Knebe A., Power C., Robotham A. S. G., Garcia-Bellido J., 2015, *MNRAS*, **450**, 1856  
 Balaguera-Antolínez A., Kitaura F.-S., Pellejero-Ibáñez M., Zhao C., Abel T., 2019, *MNRAS*, **483**, L58  
 Balaguera-Antolínez A., et al., 2020, *MNRAS*, **491**, 2565  
 Baldauf T., Seljak U., Desjacques V., McDonald P., 2012, *Phys. Rev. D*, **86**, 083540  
 Baldauf T., Seljak U., Smith R. E., Hamaus N., Desjacques V., 2013, *Phys. Rev. D*, **88**, 083507  
 Baldauf T., Mercolli L., Mirbabayi M., Pajer E., 2015, *J. Cosmology Astropart. Phys.*, **2015**, 007  
 Baldry I. K., Balogh M. L., Bower R. G., Glazebrook K., Nichol R. C., Bamford S. P., Budavari T., 2006, *MNRAS*, **373**, 469  
 Ball N. M., Loveday J., Brunner R. J., 2008, *MNRAS*, **383**, 907  
 Balogh M. L., Christlein D., Zabludoff A. I., Zaritsky D., 2001, *ApJ*, **557**, 117  
 Balogh M. L., Baldry I. K., Nichol R., Miller C., Bower R., Glazebrook K., 2004, *ApJ*, **615**, L101  
 Bardeen J. M., Bond J. R., Kaiser N., Szalay A. S., 1986, *ApJ*, **304**, 15  
 Barnes J., Efstathiou G., 1987, *ApJ*, **319**, 575  
 Baumgarten F., Chuang C.-H., 2018, *MNRAS*, **480**, 2535  
 Benitez N., Dupke R., Moles M., others 2014, arXiv e-prints, [p. arXiv:1403.5237](https://arxiv.org/abs/1403.5237)  
 Bernardeau F., 1994, *ApJ*, **427**, 51  
 Bernardeau F., Colombi S., Gaztañaga E., Scoccimarro R., 2002, *Phys. Rep.*, **367**, 1  
 Betancort-Rijo J., López-Corredoira M., 2000, *ApJ*, **534**, L117  
 Beygu B., Kreckel K., Van de Weygaert R., Van der Hulst J. M., van Gorkom J. H., 2013, *AJ*, **145**, 120  
 Binney J., Silk J., 1979, *MNRAS*, **188**, 273  
 Bladel J., 1959, IRE Transactions on Antennas and Propagation, **7**, 119  
 Blanton M. R., Eisenstein D., Hogg D. W., Schlegel D. J., Brinkmann J., 2005, *ApJ*, **629**, 143  
 Blot L., et al., 2019, *MNRAS*, **485**, 2806  
 Bond J. R., Myers S. T., 1996, *ApJS*, **103**, 1  
 Bond J. R., Kofman L., Pogosyan D., 1996, *Nature*, **380**, 603  
 Bos E. G. P., Van de Weygaert R., Dolag K., Pettorino V., 2012, *MNRAS*, **426**, 440  
 Bouchet F. R., Juszkiewicz R., Colombi S., Pellat R., 1992, *ApJ*, **394**, L5  
 Bouchet F. R., Colombi S., Hivon E., Juszkiewicz R., 1995, *A&A*, **296**, 575  
 Buchert T., 1994, *MNRAS*, **267**, 811  
 Buchert T., Ehlers J., 1993, *MNRAS*, **264**, 375  
 Casas-Miranda R., Mo H. J., Sheth R. K., Boerner G., 2002, *MNRAS*, **333**, 730  
 Catelan P., 1995, *MNRAS*, **276**, 115  
 Catelan P., Theuns T., 1996a, *MNRAS*, **282**, 436  
 Catelan P., Theuns T., 1996b, *MNRAS*, **282**, 455  
 Cautun M., Van de Weygaert R., Jones B. J. T., 2013, *MNRAS*, **429**, 1286  
 Cen R., Ostriker J. P., 1993, *ApJ*, **417**, 415  
 Chan K. C., Scoccimarro R., Sheth R. K., 2012, *Phys. Rev. D*, **85**, 083509  
 Chuang C.-H., Kitaura F.-S., Prada F., Zhao C., Yepes G., 2015, *MNRAS*, **446**, 2621  
 Chuang C.-H., Kitaura F.-S., Liang Y., Font-Ribera A., Zhao C., McDonald P., Tao C., 2017, *Phys. Rev. D*, **95**, 063528  
 Chue C. Y. R., Dalal N., White M., 2018, *Journal of Cosmology and Astro-Particle Physics*, **2018**, 012  
 Colavincenzo M., et al., 2019, *MNRAS*, **482**, 4883  
 Contreras S., Zehavi I., Padilla N., Baugh C. M., Jiménez E., Lacerna I., 2019, *MNRAS*, **484**, 1133  
 Cooray A., Sheth R., 2002, *Phys. Rep.*, **372**, 1



- Cui W., et al., 2019, *MNRAS*, **485**, 2367
- Cusin G., Tansella V., Durrer R., 2017, *Phys. Rev. D*, **95**, 063527
- De Graaff A., Cai Y.-C., Heymans C., Peacock J. A., 2019, *A&A*, **624**, A48
- De Jong R. S., Agertz O., Berbel A. A., others 2019, *The Messenger*, **175**, 3
- Dekel A., Lahav O., 1999, *ApJ*, **520**, 24
- Desjacques V., Crocce M., Scoccimarro R., Sheth R. K., 2010, *Phys. Rev. D*, **82**, 103529
- Desjacques V., Jeong D., Schmidt F., 2018, *Phys. Rep.*, **733**, 1
- Doroshkevich A. G., 1970, *Astrofizika*, **6**, 581
- Eckert D., et al., 2015, *Nature*, **528**, 105
- Eggemeier A., Scoccimarro R., Smith R. E., 2019, *Phys. Rev. D*, **99**, 123514
- Eggemeier A., Scoccimarro R., Smith R. E., Crocce M., Pezzotta A., Sánchez A. G., 2021, *Phys. Rev. D*, **103**, 123550
- Elia A., Kulkarni S., Porciani C., Pietroni M., Matarrese S., 2011, *MNRAS*, **416**, 1703
- Falck B. L., Neyrinck M. C., Szalay A. S., 2012, *ApJ*, **754**, 126
- Fang F., Forero-Romero J., Rossi G., Li X.-D., Feng L.-L., 2019, *MNRAS*, **485**, 5276–5284
- Feldbrugge J., Van de Weygaert R., Hidding J., Feldbrugge J., 2018, *J. Cosmology Astropart. Phys.*, **2018**, 027
- Feldman H. A., Kaiser N., Peacock J. A., 1994, *ApJ*, **426**, 23
- Filho M. E., Sánchez Almeida J., Muñoz-Tuñón C., Nuza S. E., Kitaura F., Heß S., 2015, *ApJ*, **802**, 82
- Fisher J. D., Faltenbacher A., 2018, *MNRAS*, **473**, 3941
- Forero-Romero J. E., Hoffman Y., Gottlöber S., Klypin A., Yepes G., 2009, *MNRAS*, **396**, 1815
- Frisch U., Matarrese S., Mohayaee R., Sobolevski A., 2002, *Nature*, **417**, 260
- Fry J. N., Gaztanaga E., 1993, *ApJ*, **413**, 447
- Fry J. N., Peebles P. J. E., 1978, *ApJ*, **221**, 19
- Fujita T., Vlah Z., 2020, *J. Cosmology Astropart. Phys.*, **2020**, 059
- Ganeshaiyah Veena P., Cautun M., Tempel E., Van de Weygaert R., Frenk C. S., 2019, *MNRAS*, **487**, 1607
- Gao L., White S. D. M., 2007, *MNRAS*, **377**, L5
- Génova-Santos R., Atrio-Barandela F., Kitaura F. S., Mücke J. P., 2015, *ApJ*, **806**, 113
- Gil-Marín H., Percival W. J., Verde L., Brownstein J. R., Chuang C.-H., Kitaura F.-S., Rodríguez-Torres S. A., Olmstead M. D., 2017, *MNRAS*, **465**, 1757
- Gramann M., 1993, *ApJ*, **405**, 449
- Grieb J. N., Sánchez A. G., Salazar-Albornoz S., Dalla Vecchia C., 2016, *MNRAS*, **457**, 1577
- Hahn O., Porciani C., Carollo C. M., Dekel A., 2007, *MNRAS*, **375**, 489
- Hahn O., Angulo R. E., Abel T., 2015, *MNRAS*, **454**, 3920
- Han J., Li Y., Jing Y., Nishimichi T., Wang W., Jiang C., 2019, *MNRAS*, **482**, 1900
- He S., Li Y., Feng Y., Ho S., Ravanbakhsh S., Chen W., Póczos B., 2019, *Proceedings of the National Academy of Science*, **116**, 13825
- Heavens A., Peacock J., 1988, *MNRAS*, **232**, 339
- Hidding J., Shandarin S. F., Van de Weygaert R., 2014, *MNRAS*, **437**, 3442
- Hoffman Y., 1988, *ApJ*, **329**, 8
- Hoffman Y., Metuki O., Yepes G., Gottlöber S., Forero-Romero J. E., Libeskind N. I., Knebe A., 2012, *MNRAS*, **425**, 2049
- Izard A., Crocce M., Fosalba P., 2016, *MNRAS*, **459**, 2327
- Jasche J., Wandelt B. D., 2013, *MNRAS*, **432**, 894
- Jeffreys H., 1939, *The Theory of Probability*. Oxford Classic Texts in the Physical Sciences
- Kaiser N., 1984, *ApJ*, **284**, L9
- Kauffmann G., White S. D. M., Heckman T. M., Ménard B., Brinchmann J., Charlot S., Tremonti C., Brinkmann J., 2004, *MNRAS*, **353**, 713
- Kitaura F. S., 2013, *MNRAS*, **429**, L84
- Kitaura F.-S., Angulo R. E., 2012, *MNRAS*, **425**, 2443
- Kitaura F.-S., Angulo R. E., Hoffman Y., Gottlöber S., 2012, *MNRAS*, **425**, 2422
- Kitaura F.-S., Yepes G., Prada F., 2014, *MNRAS*, **439**, L21
- Kitaura F.-S., Gil-Marín H., Scóccola C. G., Chuang C.-H., Müller V., Yepes G., Prada F., 2015, *MNRAS*, **450**, 1836
- Kitaura F.-S., et al., 2016a, *Phys. Rev. Lett.*, **116**, 171301
- Kitaura F.-S., et al., 2016b, *MNRAS*, **456**, 4156
- Koda J., Blake C., Beutler F., Kazin E., Marin F., 2016, *MNRAS*, **459**, 2118
- Kodi Ramanah D., Charnock T., Lavaux G., 2019, *Phys. Rev. D*, **100**, 043515
- Kokron N., DeRose J., Chen S.-F., White M., Wechsler R. H., 2021, *MNRAS*, **505**, 1422
- Kovács A., Sánchez C., García-Bellido J., others 2019, *MNRAS*, **484**, 5267
- Kravtsov A. V., Klypin A. A., 1999, *ApJ*, **520**, 437
- Kreckel K., van Gorkom J. H., Beygu B., Van de Weygaert R., Van der Hulst J. M., Aragon-Calvo M. A., Peletier R. F., 2016, in Van de Weygaert R., Shandarin S., Saar E., Einasto J., eds, *IAU Symposium Vol. 308, The Zeldovich Universe: Genesis and Growth of the Cosmic Web*. pp 591–599, doi:10.1017/S1743921316010644
- Lavaux G., Wandelt B. D., 2010, *MNRAS*, **403**, 1392
- Lazeyras T., Schmidt F., 2018, *J. Cosmology Astropart. Phys.*, **2018**, 008
- Lazeyras T., Musso M., Schmidt F., 2017, *Journal of Cosmology and Astro-Particle Physics*, **2017**, 059
- Lee J., Lee B., 2008, *ApJ*, **688**, 78
- Levi M., et al., 2013, preprint, ([arXiv:1308.0847](https://arxiv.org/abs/1308.0847))
- Liang Y., Zhao C., Chuang C.-H., Kitaura F.-S., Tao C., 2016, *MNRAS*, **459**, 4020
- Libeskind N. I., Hoffman Y., Knebe A., Steinmetz M., Gottlöber S., Metuki O., Yepes G., 2012, *MNRAS*, **421**, L137
- Libeskind N. I., et al., 2018, *MNRAS*, **473**, 1195
- Lippich M., et al., 2019, *MNRAS*, **482**, 1786
- Lu T. H.-C., Ananda K., Clarkson C., Maartens R., 2009, *J. Cosmology Astropart. Phys.*, **2009**, 023
- Matarrese S., Verde L., Heavens A. F., 1997, *MNRAS*, **290**, 651
- Mathuriya A., et al., 2018, arXiv e-prints, p. [arXiv:1808.04728](https://arxiv.org/abs/1808.04728)
- Matsubara T., 1999, *ApJ*, **525**, 543
- Matsubara T., 2008, *Phys. Rev. D*, **77**, 063530
- McDonald P., 2006, *Phys. Rev. D*, **74**, 103512
- McDonald P., Roy A., 2009, *J. Cosmology Astropart. Phys.*, **2009**, 020
- Mirbabayi M., Schmidt F., Zaldarriaga M., 2015, *J. Cosmology Astropart. Phys.*, **2015**, 030
- Mo H. J., White S. D. M., 1996, *MNRAS*, **282**, 347
- Mo H., Van den Bosch F. C., White S., 2010, *Galaxy Formation and Evolution*
- Modi C., Castorina E., Seljak U., 2017, *MNRAS*, **472**, 3959
- Monaco P., Theuns T., Taffoni G., 2002a, *MNRAS*, **331**, 587
- Monaco P., Theuns T., Taffoni G., Governato F., Quinn T., Stadel J., 2002b, *ApJ*, **564**, 8
- Munshi D., 2018, *J. Cosmology Astropart. Phys.*, **2018**, 053
- Nadathur S., Carter P., Percival W. J., 2018, *Monthly Notices of the Royal Astronomical Society*, **482**, 2459
- Nadler E. O., Perko A., Senatore L., 2018, *J. Cosmology Astropart. Phys.*, **2018**, 058
- Naidoo K., Whiteway L., Massara E., Gualdi D., Lahav O., Viel M., Gil-Marín H., Font-Ribera A., 2019, *MNRAS*, **491**, 1709–1726
- Neyrinck M. C., Aragón-Calvo M. A., Jeong D., Wang X., 2014, *MNRAS*, **441**, 646
- Nickalls R. W. D., 1993, *The Mathematical Gazette*, **77**, 354–359
- Nusser A., Branchini E., 2000, *MNRAS*, **313**, 587
- Nusser A., Dekel A., 1992, *ApJ*, **391**, 443

- Nuza S. E., Kitaura F.-S., Heß S., Libeskind N. I., Müller V., 2014, *MNRAS*, **445**, 988
- Pajer E., Zaldarriaga M., 2013, *J. Cosmology Astropart. Phys.*, **2013**, 037
- Pan D. C., Vogeley M. S., Hoyle F., Choi Y.-Y., Park C., 2012, *MNRAS*, **421**, 926
- Paranjape A., Hahn O., Sheth R. K., 2018, *MNRAS*, **476**, 3631
- Park D., Lee J., 2007, *Phys. Rev. Lett.*, **98**, 081301
- Peacock J. A., Heavens A. F., 1985, *MNRAS*, **217**, 805
- Peebles P. J. E., 1980, The large-scale structure of the universe
- Peebles P. J. E., 1989, *ApJ*, **344**, L53
- Pellejero-Ibañez M., et al., 2020, *MNRAS*, **493**, 586
- Pichon C., Bernardeau F., 1999, *A&A*, **343**, 663
- Pierpaoli C., Basser P. J., 1996, Magnetic resonance in medicine, **36**, 893
- Pisani A., Sutter P. M., Hamaus N., Alizadeh E., Biswas R., Wandelt B. D., Hirata C. M., 2015, *Phys. Rev. D*, **92**, 083531
- Pollack J. E., Smith R. E., Porciani C., 2012, *MNRAS*, **420**, 3469
- Pollack J. E., Smith R. E., Porciani C., 2014, *MNRAS*, **440**, 555
- Porciani C., Dekel A., Hoffman Y., 2002a, *MNRAS*, **332**, 325
- Porciani C., Dekel A., Hoffman Y., 2002b, *MNRAS*, **332**, 339
- Porto R. A., Senatore L., Zaldarriaga M., 2014, *J. Cosmology Astropart. Phys.*, **2014**, 022
- Press W. H., Schechter P., 1974, *ApJ*, **187**, 425
- Press W., Teukolsky S., Vetterling W., Flannery B., 2007, Numerical Recipes: The Art of Scientific Computing, 3 edn. Cambridge University Press, <http://nr.com/>
- Rajagopalan V., Jiang Z., Yue G., Radic J., Piro E., Wylie G., Das A., 2017, *Brain Disorders & Therapy*, **06**
- Ramakrishnan S., Paranjape A., Hahn O., Sheth R. K., 2019, *MNRAS*, **489**, 2977
- Saito S., Baldauf T., Vlah Z., Seljak U., Okumura T., McDonald P., 2014, *Phys. Rev. D*, **90**, 123522
- Saslaw W. C., Hamilton A. J. S., 1984, *ApJ*, **276**, 13
- Schmidt F., Jeong D., Desjacques V., 2013, *Phys. Rev. D*, **88**, 023515
- Schmittfull M., Simonović M., Assassi V., Zaldarriaga M., 2019, *Phys. Rev. D*, **100**, 043514
- Schröder J., Neff P., (service) S. O., 2010., Poly-, Quasi- and Rank-One Convexity in Applied Mechanics. CISM International Centre for Mechanical Sciences., Springer Vienna., Vienna ; <http://dx.doi.org/10.1007/978-3-7091-0174-2>
- Scoccimarro R., Sheth R. K., 2002, *MNRAS*, **329**, 629
- Scoccimarro R., Hui L., Manera M., Chan K. C., 2012, *Phys. Rev. D*, **85**, 083002
- Sefusatti E., Komatsu E., 2007, *Phys. Rev. D*, **76**, 083004
- Seljak U., 2000, *MNRAS*, **318**, 203
- Senatore L., 2015, *J. Cosmology Astropart. Phys.*, **2015**, 007
- Senatore L., Zaldarriaga M., 2015, *J. Cosmology Astropart. Phys.*, **2015**, 013
- Shandarin S., Habib S., Heitmann K., 2012, *Phys. Rev. D*, **85**, 083005
- Sheth R. K., 1995, *MNRAS*, **274**, 213
- Sheth R. K., Lemson G., 1999, *MNRAS*, **304**, 767
- Sheth R. K., Tormen G., 1999, *MNRAS*, **308**, 119
- Sheth R. K., Tormen G., 2002, *MNRAS*, **329**, 61
- Sheth R. K., Van de Weygaert R., 2004, *MNRAS*, **350**, 517
- Sheth R. K., Chan K. C., Scoccimarro R., 2013, *Phys. Rev. D*, **87**, 083002
- Shi J., Sheth R. K., 2018, *MNRAS*, **473**, 2486
- Shi Y., Cautun M., Li B., 2018, *Phys. Rev. D*, **97**, 023505
- Sinigaglia F., Kitaura F.-S., Balaguera-Antolínez A., Nagamine K., Ata M., Shimizu I., Sánchez-Benavente M., 2021, *ApJ*, **921**, 66
- Smith R. E., Scoccimarro R., Sheth R. K., 2007, *Phys. Rev. D*, **75**, 063512
- Somerville R. S., Lemson G., Sigad Y., Dekel A., Kauffmann G., White S. D. M., 2001, *MNRAS*, **320**, 289
- Sousbie T., Pichon C., Colombi S., Novikov D., Pogosyan D., 2008, *MNRAS*, **383**, 1655
- Sousbie T., Pichon C., Kawahara H., 2011, *MNRAS*, **414**, 384
- Springel V., White S. D. M., Tormen G., Kauffmann G., 2001, *MNRAS*, **328**, 726
- Stein G., Alvarez M. A., Bond J. R., 2019, *MNRAS*, **483**, 2236
- Szalay A. S., 1988, *ApJ*, **333**, 21
- Tempel E., Stoica R. S., Martínez V. J., Liivamägi L. J., Castellan G., Saar E., 2014, *MNRAS*, **438**, 3465
- Tinker J. L., Robertson B. E., Kravtsov A. V., Klypin A., Warren M. S., Yepes G., Gottlöber S., 2010, *ApJ*, **724**, 878
- Vakili M., Kitaura F.-S., Feng Y., Yepes G., Zhao C., Chuang C.-H., Hahn C., 2017, *MNRAS*, **472**, 4144
- Valageas P., 2011, *A&A*, **525**, A98
- Van de Weygaert R., Bond J. R., 2008, Clusters and the Theory of the Cosmic Web. p. 335, [doi:10.1007/978-1-4020-6941-3\\_10](https://doi.org/10.1007/978-1-4020-6941-3_10)
- Van de Weygaert R., Schaap W., 2009, The Cosmic Web: Geometric Analysis. pp 291–413, [doi:10.1007/978-3-540-44767-2\\_11](https://doi.org/10.1007/978-3-540-44767-2_11)
- Vogelsberger M., White S. D. M., 2011, *MNRAS*, **413**, 1419
- Vogelsberger M., White S. D. M., Helmi A., Springel V., 2008, *MNRAS*, **385**, 236
- Wang H., Mo H. J., Yang X., Van den Bosch F. C., 2013, *ApJ*, **772**, 63
- Weisstein E. W., 2002, CRC Concise Encyclopedia of Mathematics. Chapman & Hall : CRC Press, Boca Raton, FL
- Werner K. F., Porciani C., 2020, *MNRAS*, **492**, 1614
- White S. D. M., 1984, *ApJ*, **286**, 38
- White S. D. M., Rees M. J., 1978, *MNRAS*, **183**, 341
- White S. D. M., Vogelsberger M., 2009, *MNRAS*, **392**, 281
- White M., Tinker J. L., McBride C. K., 2014, *MNRAS*, **437**, 2594
- Wu Z., et al., 2021, *ApJ*, **913**, 2
- Yang X., et al., 2017, *ApJ*, **848**, 60
- Zeldovich Y. B., 1970, *A&A*, **500**, 13
- Zennaro M., Angulo R. E., Pellejero-Ibañez M., Stücker J., Contreras S., Aricó G., 2021, arXiv e-prints, p. [arXiv:2101.12187](https://arxiv.org/abs/2101.12187)
- Zhang X., Wang Y., Zhang W., Sun Y., He S., Contardo G., Villaescusa-Navarro F., Ho S., 2019, arXiv e-prints, p. [arXiv:1902.05965](https://arxiv.org/abs/1902.05965)
- Zhao C., Kitaura F.-S., Chuang C.-H., Prada F., Yepes G., Tao C., 2015, *MNRAS*, **451**, 4266
- Zhao C., et al., 2020, *MNRAS*, **491**, 4554

## APPENDIX A: RELATION BETWEEN THE INVARIANTS AND THE COSMIC WEB CLASSIFICATION

In this appendix we study the relation between the cosmic web classification and the invariants of the tidal field tensor, defined in Eq. (17).

In particular, we consider different cases based on the I-web restricted to the information provided by  $I_1$ ,  $I_2$ , and  $I_3$  (we also consider without loss of generality a threshold eigenvalue of zero, as in Hahn et al. 2007):

- $I_3 > 0$ :  $\lambda_1 \lambda_2 \lambda_3 > 0$ , which leaves two options, either knots:  $\{\lambda_i > 0 \forall i\}$ , or sheets:  $\{\lambda_1 > 0, \lambda_i < 0 \text{ for } i = 2, 3\}$

–  $I_2 < 0$ :  $\lambda_1 \lambda_2 + \lambda_1 \lambda_3 + \lambda_2 \lambda_3 < 0$ . Since  $\lambda_1 > 0$  for both knots and sheets, we can multiply with  $\lambda_1$ , hence obtaining:  $\lambda_1 \lambda_2 \lambda_3 + \lambda_1^2 \lambda_2 + \lambda_1^2 \lambda_3 < 0$ , but since  $I_3 > 0$ , it follows that  $\lambda_3 < -\lambda_2$ . This is only accomplished for sheets.

–  $I_2 > 0$  is equivalent to  $I_1 > \lambda_1 - \lambda_2 \lambda_3 / \lambda_1$ . On the other hand  $I_1 > \lambda_1$  for knots, but  $I_1 < \lambda_1$  for sheets, since for such cosmic web types  $\lambda_2 + \lambda_3 < 0$ .

- $I_3 < 0$ :  $\lambda_1\lambda_2\lambda_3 < 0$ , i.e., either voids:  $\{\lambda_i < 0 \forall i\}$ , or filaments:  $\{\lambda_i > 0, \text{ for } i = 1, 2, \lambda_3 < 0\}$ 
  - $I_2 < 0$ : since for both cases  $\lambda_1\lambda_2 > 0$ , we have  $\lambda_1\lambda_3 + \lambda_2\lambda_3 < 0$ . Also, for both  $\lambda_3 < 0$ . Thus,  $\lambda_1 > -\lambda_2$ , which is only accomplished for filaments.
  - $I_2 > 0$ : Since for both  $\lambda_3 < 0$ , we get  $I_1 < \lambda_3 - \lambda_2\lambda_3/\lambda_1$ . On the other hand, for voids  $\lambda_1 + \lambda_2 < 0$ , hence,  $I_1 < \lambda_3$ . And for filaments  $\lambda_1 + \lambda_2 > 0$  yielding  $I_1 > \lambda_3$ .

In summary, the connection between the T-web and the I-web in terms of the invariants of the tidal field tensor is given by:

- knots:  $I_3 > 0 \ \& \ I_2 > 0 \ \& \ I_1 > \lambda_1$
- filaments:  $I_3 < 0 \ \& \ I_2 < 0 \ || \ I_3 < 0 \ \& \ I_2 > 0 \ \& \ \lambda_3 < I_1 < \lambda_3 - \lambda_2\lambda_3/\lambda_1$
- sheets:  $I_3 > 0 \ \& \ I_2 < 0 \ || \ I_3 > 0 \ \& \ I_2 > 0 \ \& \ \lambda_1 - \lambda_2\lambda_3/\lambda_1 < I_1 < \lambda_1$
- voids:  $I_3 < 0 \ \& \ I_2 > 0 \ \& \ I_1 < \lambda_1$

The introduction of a threshold other than zero will shift these relations. One should note, that the classification into different cosmic web types apparently requires the specification of certain eigenvalues, but if the density  $I_1$  is known over its whole range of values, the combination with the sign of the other two invariants ( $I_2$  and  $I_3$ ) fully constrains the dif-

ferent cases. In any case, from the characteristic polynomial each eigenvalue can be computed with the knowledge over the first three invariants. What has been found here also applies to the velocity shear classification (V-web) by substituting the tidal field tensor with the shear tensor. The difference is that the V-web based on the velocity field beyond linear theory, effectively includes additional terms which we classified into the  $F_{\text{shear}}(\vec{v}(\vec{r}))$  and  $F_{\text{curl}}(\vec{v}(\vec{r}))$  terms in Eq. (16), as we investigate in §5.1.1.

It is interesting to note, non-theless, that the T-web (and V-web) has been a useful tool, as it carries more information than the density alone, involving the second order non-local bias  $I_4$  (through  $\delta$  and  $I_2$ ), and partial information on the third order  $s^3$  term. However, from these calculations we find that the T-web (and V-web) constrains only a sub-region of the parameter space spanned by the I-web, involving only  $I_1, I_2, I_3$  for very restricted cases. Thus the T-web cannot account for anisotropic dependencies such as ellipticity, prolateness, or the anisotropic parameter. It can neither account for the non-local bias terms  $\delta s^2$ , nor properly for  $s^3$ , since  $I_5$  is not constrained by the T-web classification.

This paper has been typeset from a  $\text{\TeX}/\text{\LaTeX}$  file prepared by the author.